LIMNOLOGY
and
OCEANOGRAPHY: METHODS

ASLO

Limnol. Oceanogr.: Methods 13, 2015, 267–287

doi: 10.1002/lom3.10024

A new methodology for quantifying bubble flow rates in deep water using splitbeam echosounders: Examples from the Arctic offshore NW-Svalbard

M. Veloso,*[1] J. Greinert,[1,2,3] J. Mienert,[4] M. De Batist[1]

[1]Renard Centre of Marine Geology, Ghent University, Ghent, Belgium
[2]GEOMAR Helmholtz Centre for Ocean Research Kiel, Department of Geology and Soil Science, Kiel, Germany
[3]Royal Netherlands Institute for Sea Research (NIOZ), Marine Biogeochemistry Division, DeepSea Monitoring Group, Den Burg, Texel, Netherlands
[4]CAGE – Centre for Arctic Gas Hydrate, Environment and Climate, Department of Marine Geology and Chemical Oceanography (GCO), UiT The Arctic University of Norway, Tromsø, Norway

Abstract

Quantifying marine methane fluxes of free gas (bubbles) from the seafloor into the water column is of importance for climate related studies, for example, in the Arctic, reliable methodologies are also of interest for studying man-made gas and oil leakage systems at hydrocarbon production sites. Hydroacoustic surveys with singlebeam and nowadays also multibeam systems have been proven to be a successful approach to detect bubble release from the seabed. A number of publications used singlebeam echosounder data to indirectly quantify free gas fluxes via empirical correlations between gas fluxes observed at the seafloor and the hydroacoustic response. Others utilize the hydroacoustic information in an inverse modeling approach to derive bubble fluxes. Here, we present an advanced methodology using data from splitbeam echosounder systems for analyzing gas release water depth (>100 m). We introduce a new MATLAB-based software for processing and interactively editing data and we present how bubble-size distribution, bubble rising speed and the model used for calculating the backscatter response of single bubbles influence the final gas flow rate calculations. As a result, we highlight the need for further investigations on how large, wobbly bubbles, bubble clouds, and multi-scattering influence target strength. The results emphasize that detailed studies of bubble-size distributions and rising speeds need to be performed in parallel to hydroacoustic surveys to achieve realistic mediated methane flow rate and flux quantifications.

Introduction

Because unique ecosystems thrive in direct proximity to methane release sites, but also because methane is a greenhouse gas that creates a positive climate warming feedback when reaching the atmosphere, methane release in the marine environment has been studied for several decades now. Recent publications about "massive" methane releases from the Eastern Siberian Arctic Shelf (Shakhova et al. 2014) highlight the need for a standardized methodology for free gas flux quantifications.

This article provides a brief review of how "large" bubbles released from seep sites can be detected and analyzed with single-beam echosounder systems (SBES) and it presents an advanced methodology to quantify bubble flow rates.

Reports on "plumes" or "hydroacoustic plumes" seen on various hydroacoustic systems date back to the 1980s, sometimes not linking the "plumes" clearly to their bubble origin (Merewether et al. 1985; Paull et al. 1995; Lewis and Marshall 1996). Studies in the Black Sea (Polikarpov 1989; Naudts et al. 2006), the Sea of Okhotsk (Obzhirov et al. 2004), Hydrate Ridge (Heeschen et al. 2003), the Barents Sea (Sauter et al. 2006, Chand et al. 2012), the Framstrait offshore NW Svalbard (Smith et al. 2014), Lake Baikal (Granin et al. 2012), the Gulf of Mexico (Solomon et al. 2009; Talukder et al. 2013; Weber et al. 2014), and the area offshore Santa Barbara (Hornafius et al. 1999; Leifer and Culling 2010) underline the usefulness of SBES observations to find active seep sites, map

Additional Supporting Information may be found in the online version of this article.

*Correspondence: MarioEnrique.VelosoAlarcon@UGent.be

their extent and even get an idea of their temporal variability (Quigley et al. 1999; Greinert et al. 2006). First attempts to quantify gas flow rates from SBES were difficult because of limitations of digital data storage capacity (Hornafius et al. 1999) and computer power for data processing. Today, this is not a problem anymore and singlebeam as well as multibeam water column data (Nikolovska et al. 2008; Lorenson et al. 2011; Weber et al. 2013) are commonly used to visualize gas release and increasingly more often to quantify gas flow rates and fluxes (Granin et al. 2012; Römer et al. 2012b).

Successful attempts have been made to measure free gas flow rates at the seafloor and model the transport toward the sea surface or into the mixed layer (Leifer and Patro 2002; Greinert et al. 2010; Schneider Von Deimling et al. 2011), accounting for gas dissolution while bubbles rise (Leifer and Patro 2002; McGinnis et al. 2006; Rehder et al. 2009). In those attempts, the amount of gas reaching the mixed layer (where it ultimately equilibrates with the atmosphere) was between 4% and 19% of the initially released gas in water depths of less than 100 m. The total methane flux shows large variations, depending on seep area, bubble sizes, and bubble release intensity. Flow rates range from 1.5 to 18.5×10^6 mol/yr for the respective areas; much higher fluxes have been presented for the Eastern Siberian Arctic Shelf (Shakhova and Semiletov 2007; Shakhova et al. 2014) or the Gulf of Mexico (Solomon et al. 2008).

Although the number of such research activities concerned with flow rate and flux estimates is currently increasing, the total amount of methane reaching the atmosphere from marine seep sources is far from being reliably determined. Also, estimates from basic modeling approaches have limited data for validation, particularly in Arctic areas (Archer et al. 2009; Biastoch et al. 2011). Extrapolations over large areas need to be made with great caution as local environmental conditions that are highly variable (temperature, depth, wind and wave activity, ice cover) is distinctly influencing flow rates.

Here, we present a methodology that allows SBES-based flow rate estimates in water depth of more than > 100 m, where no or a very limited release of single bubbles can be observed during ship-based SBES surveys. Our approach provides an easy-to-use methodology allowing a better comparison of data from repeated surveys and/or groups for analyzing long-term changes in methane flow rates and fluxes from the ocean floor through the water column.

Bubble detection in SBES echograms

How bubbles look like in echograms

The approach for detecting and quantifying free gas is based on SBE data recorded with a splitbeam system. For the correct detection of single bubbles and bubble clouds, the recognition and classification of different backscattering targets in the water column is essential. Slow sailing speed (< 5 kn) and a "silent" ship with additional acoustic sources being turned off (e.g., multibeam systems, sub-bottom profilers) significantly enhance the quality of data and the opportunity to discriminate bubbles from other signals such as fish, fish larvae, plankton, or suspended sediment. The recognition of free gas release essentially depends on the pattern of the backscattering in echograms (Greinert et al. 2006; Judd and Hovland 2007). Because of the typical "flare" shape in echograms (for non-single bubbles), these features are referred to as "flares" (Greinert et al. 2006; Römer et al. 2012a, b), but the term "bubble plume" or "hydroacoustic plume of bubbles" is also used (e.g., Westbrook et al. 2009; Fig. 1 and 2).

How large bubbles (> 1 mm in diameter) in the water column can be identified and distinguished from other signal sources has been described previously (e.g., Judd et al. 1997; Greinert et al. 2006). The visual representation of bubbles in echograms strongly depends on vessel speed, water currents influencing the bubble rising path, and on how the bubbles have been insonified by the acoustic beam (Fig. 2). As echograms are usually displays of echo intensity per depth (y-axis) over time (x-axis) different vertical exaggeration might stretch fish schools in the y-axis that can result in false flare detection. "Rooted" flares (Fig. 2d,e) and the observation of single bubbles rising (Fig. 2f) give ultimate proof.

Side lobe effects specific to different transducers may clearly show in echograms if the backscattering of the target is strong enough. One example is given in Fig. 3; others have been presented by, for example, Nikolovska et al. (2008) and Schneider Von Deimling et al. (2011).

In comparison to the flares in Fig. 3 that were recorded at sites that more or less continuously release bubbles, backscattering of single bubbles or small bubble clouds can be reasonably well detected at a slow vessel speed (< 2 knots) and low background noise. Such conditions existed for flow rate quantifications at shallow water depths, for example, in lakes and shelf areas (Ostrovsky 2003; DelSontro et al. 2011). A single bubble or an isolated bubble cloud appears as an almost straight line with a positive slope in echograms (Fig. 4). Unfortunately, in deeper water (> 100 m) observations of single bubble targets are very limited in the literature. This is most likely due to the lack of good quality data that could track bubbles inside the acoustic beam for a high enough number of pings (over time). Being stationary at one site or going slowly helps to acquire more information from the same target with the reduced ping rate in deeper water and the increased possibility of additional backscatteres in the larger insonified water volume. As a consequence, there is a lack of bubble rising speed (BRS) measurements and bubble size estimates needed for flow rate quantifications.

It should be pointed out that faster survey speeds (~ 10 kn) would cover larger areas giving a better regional view on the distribution of gas release sites. Choosing between coverage (fast and thus wider coverage, less data per seep, more noise from the ship or sea state) and high quality data (slow and thus less coverage, less noise, more data per seep) depends on the research question (overview mapping

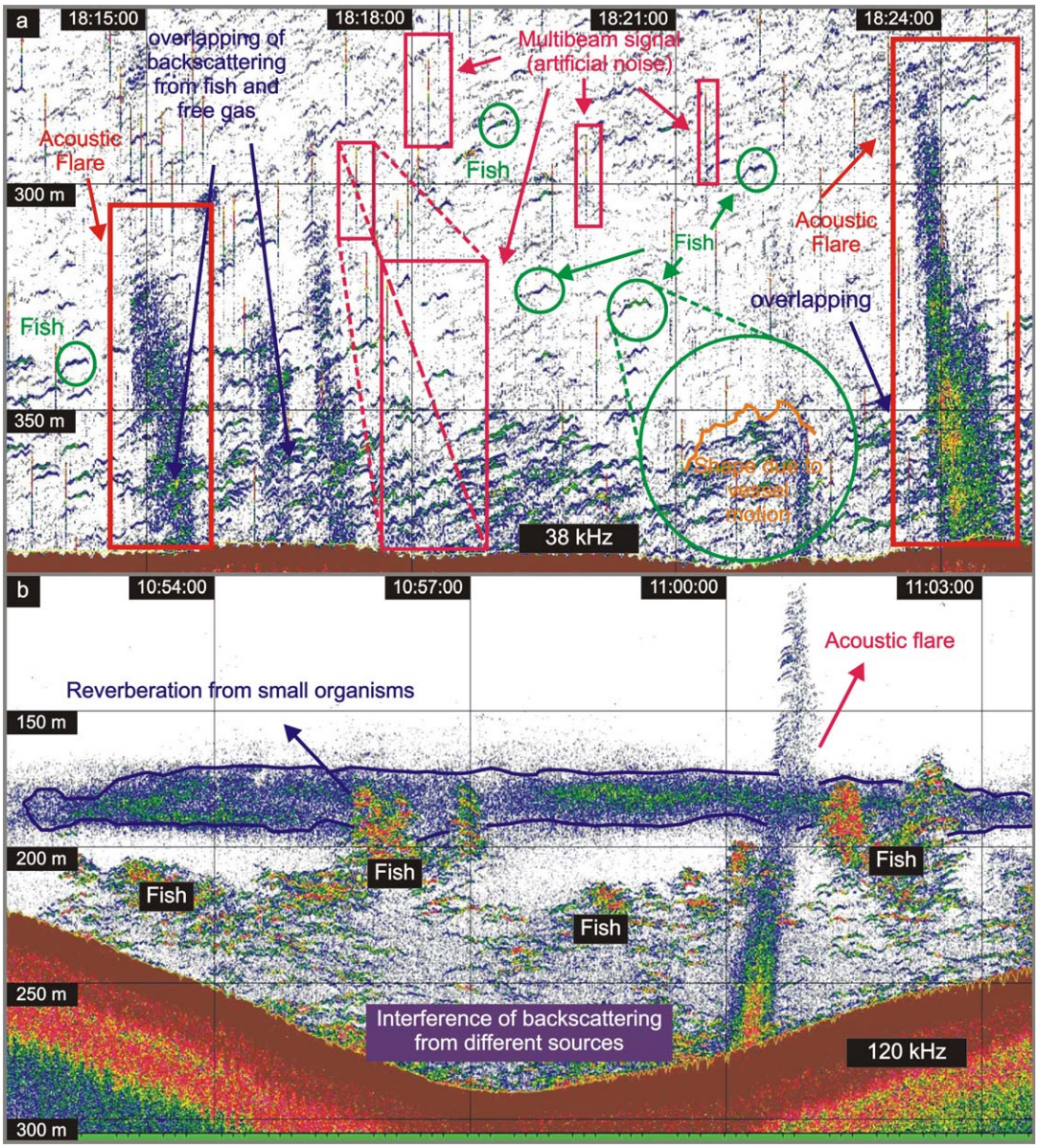

Fig. 1. (a) Echograms (38 kHz) showing flares as manifestation of rising bubbles and sources of noise (multibeam) and reverberation (fish). This complicates the identification of free gas fluxes as the interference of the different signal sources results in wrong backscattering values for bubbles, which again may result in flux overestimations. The image shows the effect of the vessel motion on the acoustic data, that is, the shape of backscatter signals of fish (wobbly shape). (b) Echogram (120 kHz) showing the interference of hydroacoustic signals from bubbles (flares) and sources of reverberation (fish and plankton). Here, the plankton layer shows more distinctly because of the higher frequency used.

vs. detailed flow rate and temporal variability studies), time and money constrains or commercial requirements.

Disturbance by noise

Fish is the main source of disturbances/reverberation during hydroacoustic bubble studies and have been observed repeatedly to interfere with flow rate estimates (Ostrovsky 2009; DelSontro et al. 2011). To obtain "pure" backscattering from bubbles, signals from fish need to be clearly identified, separated and automatically or manually removed from the data prior to quantitative processing. Single fish can be recognized by their concave shape (Lefeuvre 2002) when the fish pass the acoustic beam, but they also show artifacts depicting the vessel motion as a "wobbly" shape (*see* example Fig. 1a). Fish schools that show up as "clouds" are sometimes difficult to discriminate from strong gas release, depending on the total number of fish and the distance between them (Fig. 1b). For unambiguous identification of fish shoals, the observer needs a good understanding of the local fish populations and their behavior (Simmonds and MacLennan 2005).

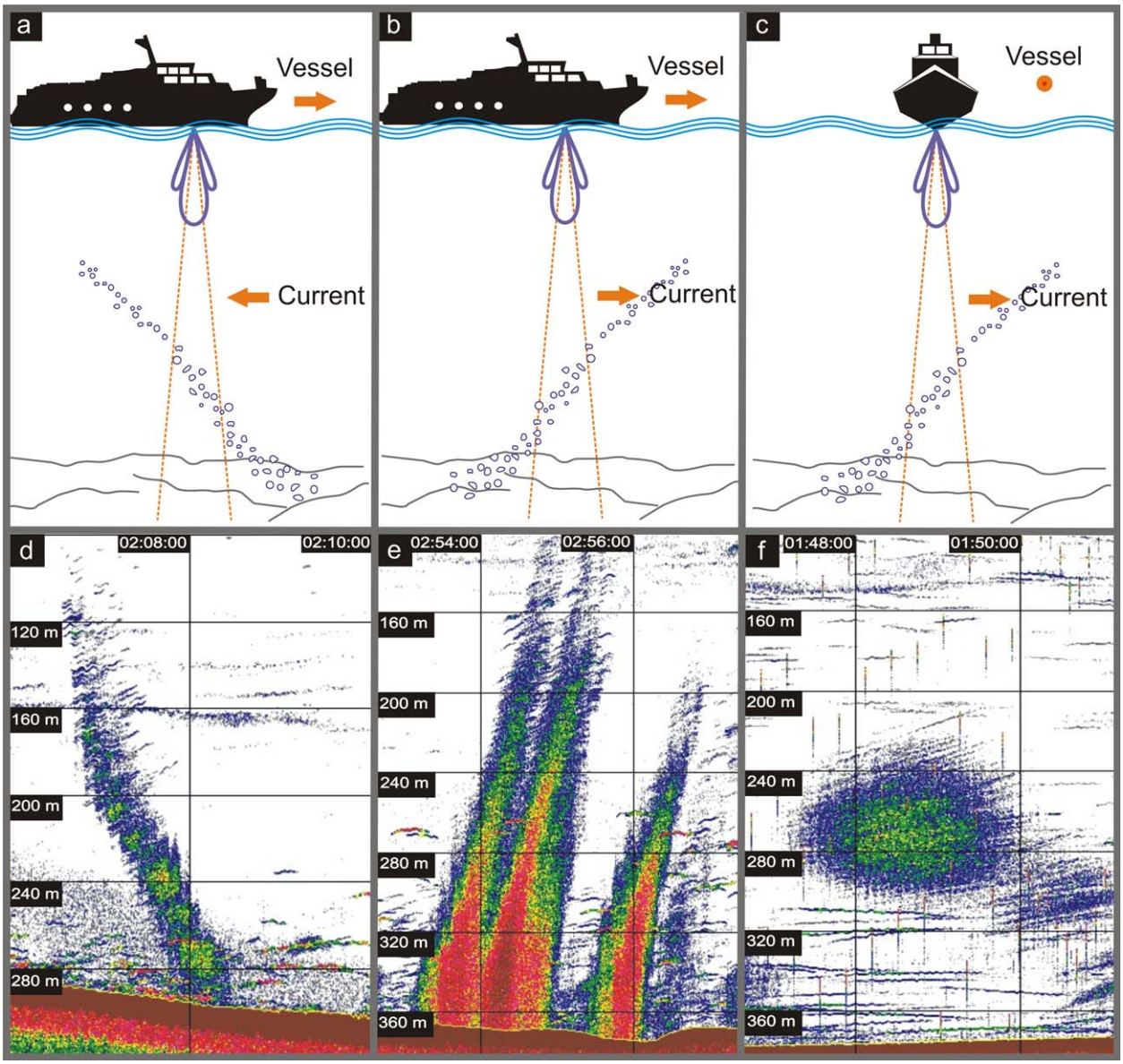

Fig. 2. Three typical examples for how bubbles influenced and shifted by currents are depicted: (a) current from the opposite direction of the ship's movement; (b) current from the same direction as the ship's movement; (c) current oblique to the ship's movement, which can easily be misinterpreted as fish or vice versa. Almost all echograms will represent a mix of two of these possibilities.

Small organisms as plankton and micronekton are another source of reverberation often accumulating in the deep scattering layer (Lurton 2002). Large amounts of small organisms cause strong echoes that could interfere with the backscattering from free gas, making quantitative analyses impossible (*see* example Fig. 1b). Plankton often concentrates at density layers increasing the backscatter signal in a certain water depth range and can influence signals from bubbles in a similar way as seafloor multiples do. A good understanding of the daily vertical migration of these microorganisms and respective adjustment of the time for data acquisition will result in better data for gas flow rate estimates. However, this might contradict monitoring efforts to estimate the gas flow or flux over tidal cycles or longer periods. Once bubbles have been identified, data need to be cleaned from noise or unwanted backscattering. This can be done by "simple" threshold filtering, speckle noise removal or manual editing in 3D space as used here.

BRS, terminal bubble rising height and influence of water currents

Gas flow rate estimates depend on several parameters such as initial gas composition, pressure and temperature conditions that affect gas density as well as bubble size and rising speed. BRSs depend on the bubble size and the amount and

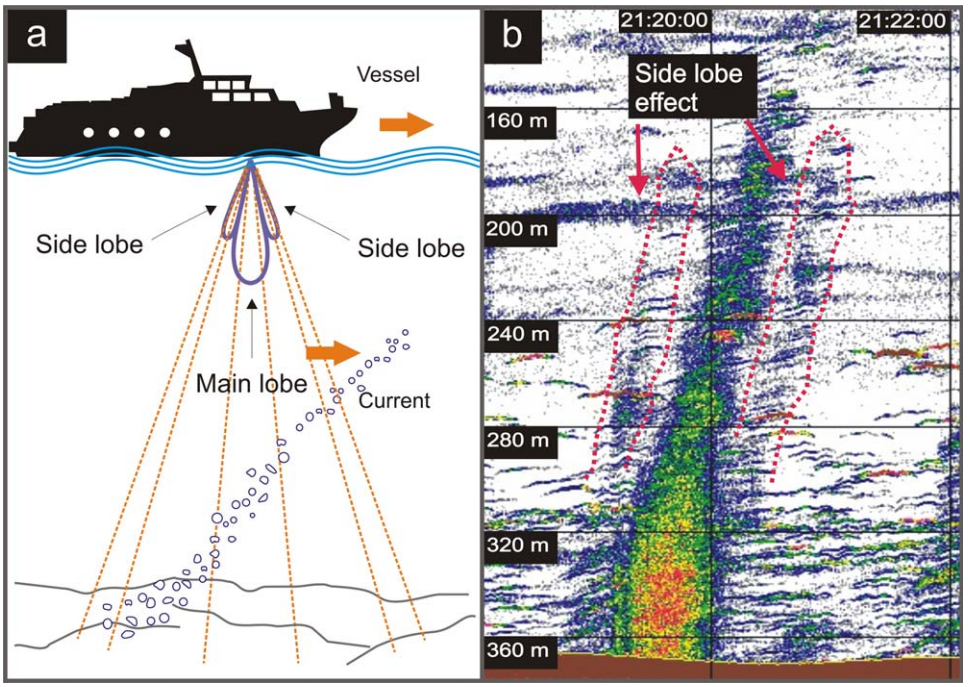

Fig. 3. Side lobe effects when rising bubbles have been insonified with the current.

kind of surfactants on the bubble surface including a potential oil or gas hydrate coating (Leifer and Patro 2002; Rehder et al. 2009, Salmi et al. 2011). Furthermore, the number of bubbles rising together influences their rising speed, as they are forming a bubble plume in which water and bubbles are upwelling together (Leifer and Culling 2010).

To estimate the BRS of single bubbles the rise path needs to be identified from echograms. The quality of the results strongly depends on the resolution of the echogram, which is related to the sampling rate of the received echo signal, the pulse length of the transmitted signal and the bandwidth during receive. In short, longer pulses as needed in greater water depth give lower resolution in the *y*-axis (depth) but shorter pulses result in more noisy data. The resolution in the *x*-axis (time axis) depends on the ping rate as function of water depth (as deeper as slower the pin grate) and the relative speed between the bubble and the moving vessel. At slow-mode sampling (< 2 kn, Ostrovsky 2009), the number of pings on the bubble target is higher, improving identification and accurate measurements of the depth change of a bubble over time (pings) without a significant effect of distance/depth changes caused by position changes inside the acoustic beam (*see* Fig. 4). Such measurements have been successfully used by several authors (Artemov 2006; Ostrovsky et al. 2008; DelSontro et al. 2011). However, in deep water the identification of single bubbles or bubble clouds is difficult and very often only the typical flares are seen, unless the ship stays stationary over one seep or is drifting very slowly (< 1 kn). This is due to the increasing foot print size of the insonified water volume and the increasing chance of recording several bubble streams simultaneously. Salmi et al (2011) present another mooring-based technique to monitor BRS and indirectly bubble sizes. The group deployed an upward-looking 200 kHz echosounder next to several bubble vents. They determined bubble size spectra from BRS measurements, assuming either clean or dirty bubbles rise behavior. Such stationary observations certainly help to understand the temporal changes in released bubble sizes as well as the activity fluctuations.

Bubbles are moved laterally by ocean currents as they rise through the water column. The horizontal displacement of a single target during a known time interval can be tracked using a splitbeam echosounder if motion, ship's heading and ray tracing are considered appropriately, assuming the horizontal displacement equals the water current speed. Using the corrected locations of the backscattered signal, georeferenced provides the direction of the water current. Figure 5a shows the horizontal current speed calculated from five bubble traces at similar water depths (Fig. 5b). In this example, all bubbles are displaced toward WNW with a speed varying from 0.5 m/s to 0.72 m/s (independent of ship's movement and heading).

As bubbles gradually dissolve as they move upward through the water column, most eventually disappear and do not reach the mixed layer or sea surface. The height at which this happens is the terminal rising height which is critical for estimating the amount of methane transported into the atmosphere/upper mixed layer. The terminal height

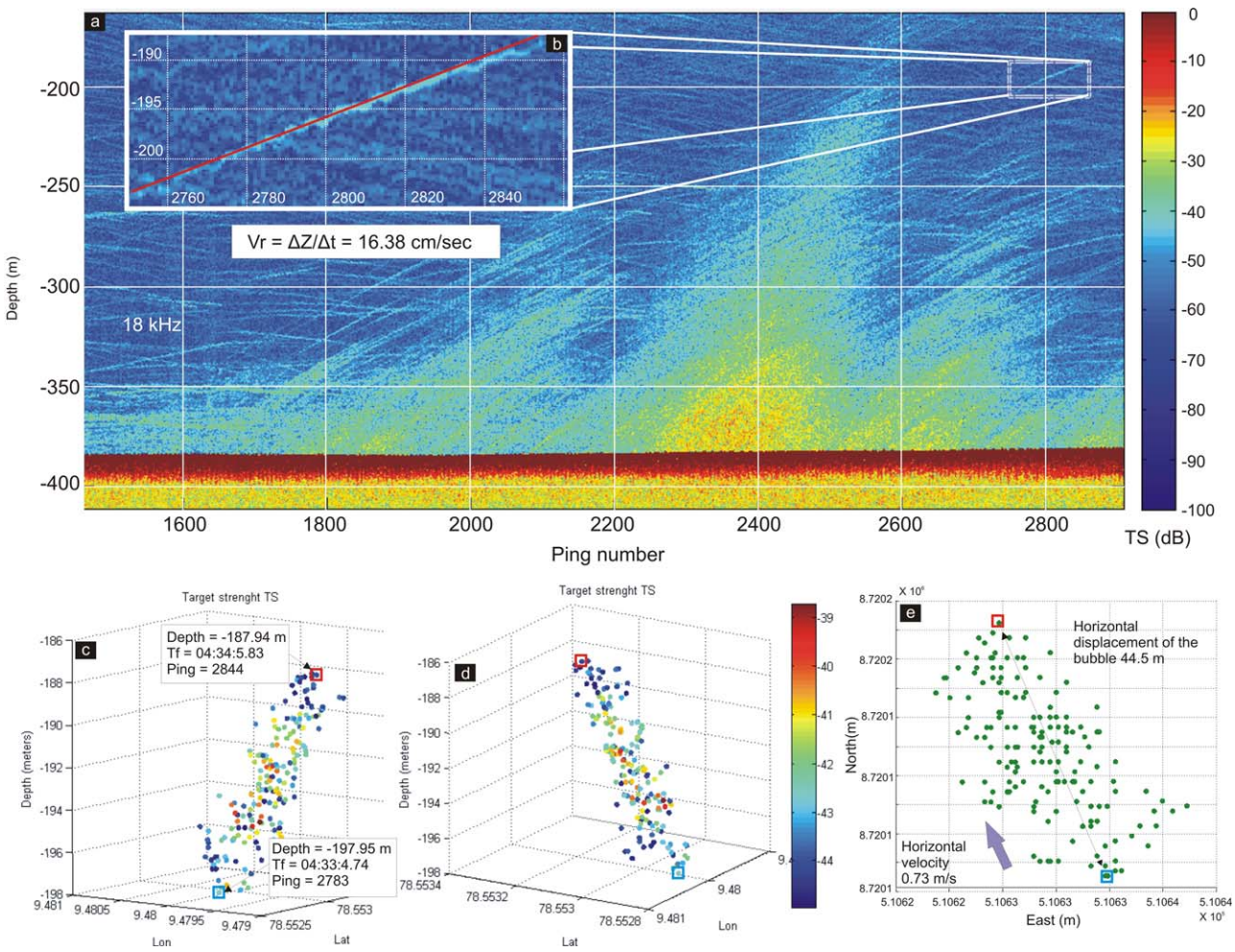

Fig. 4. (a) Echogram showing backscattering from a single bubble captured during slow-mode-sampling. (b) Enlarged signal of the rising bubble; the slight wavy pattern is caused by the ship movements (pitch, roll, heave). Images (c) and (d) show two 3D views of the backscattering positions produced by a rising bubble in a latitude-longitude-depth coordinate system. Colors in images (a), (b), (c), (d) represent the target strength (*TS*). Image (e) shows a top-down view of the spatial distribution in UTM coordinates (Zone 33). The image clearly shows the current effect that causes the horizontal displacement of the bubble for a certain time and depth interval (here ~ 0.5 m/s toward the NE).

is often derived from the height of the flare in an echogram (Römer et al. 2012a). The respective values must be used with caution because only a conical volume of the water column is insonified, due to the hydroacoustic beam pattern and the backscattering strength of bubbles decreases quickly when bubbles become smaller than the resonance frequency at a particular depth (Medwin and Clay 1998). A flare height should only be called "terminal" if all bubbles are definitely inside the acoustic lobe. Greinert et al. (2010) provide an example where transducers with different frequencies depict the terminal flare height very differently although the recording happened simultaneously. In shallow water, the chance that only parts of the rising bubble stream are insonified is high, in particular if ocean currents shift bubbles laterally away from their point of origin (Fig. 2f). Using multibeam systems overcomes this problem, but performing SBES surveys over the same seep site from different directions and comparing flare heights may also provide accurate information. Recording SBES water column data simultaneously with MBES would help to determine the terminal rising height. A disadvantage may be the introduction of additional noise in the SBES data.

Study area

The study area lies west of Prins Karls Forland (PKF) offshore NW Svalbard (Fig. 6), where two datasets have been recorded in July 2009 and 2012 onboard RV Helmer Hanssen from UiT (The Arctic University of Norway). Methane seepage offshore Svalbard has first been described by Knies et al. (2004) and later by Westbrook et al. (2009). Since then, the area has been annually revisited by several research groups. Three distinct depth intervals of bubble release have been

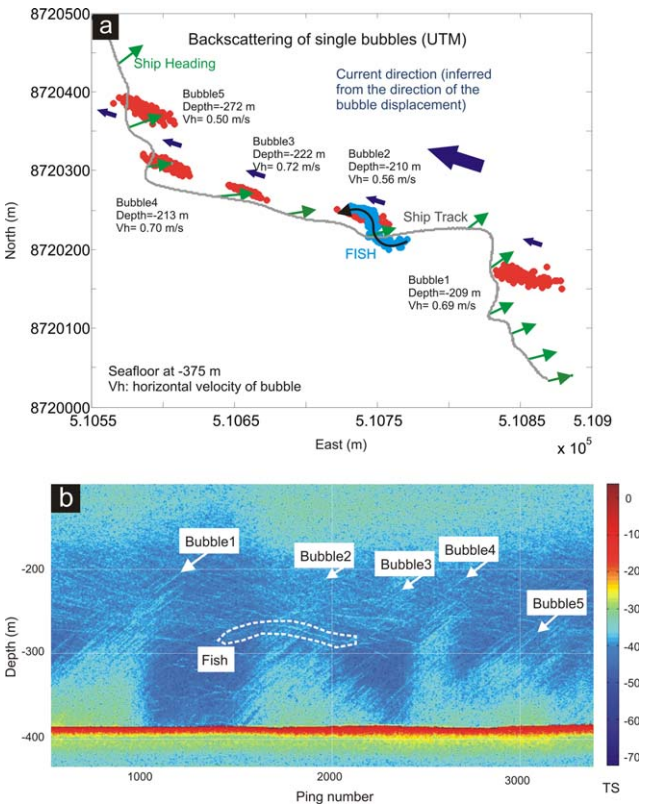

Fig. 5. Evaluation of current speed using hydroacoustic information of single bubbles captured by a splitbeam echosounder. (a) Red spots represent the position of the backscattering produced by bubbles during a certain time interval (horizontal bubble displacement). Blue arrows show the displacement direction. The track of the vessel is shown as a line with green arrows indicating the vessel heading. The horizontal speed of each bubble is specified. (b) Gas release in ~375 m water depth; the five bubble lines measured are indicated. Low angle lines that show increasing depth with ping number, are diving fish (e.g., inside dashed line).

determined. The deeper area, at about 400 m water depth, appears to be associated with the top of the gas hydrate stability zone (TGHZ) and the dissociation of gas hydrate in response to increasing bottom water temperatures (Westbrook et al. 2009). However, Berndt et al. (2014) have shown that methane release is not a short term but a long-term process, active for more than several thousand years that started after the last ice age. At shallower water depth in 240 m, focused methane-charged fluids migrate along a sedimentologically defined permeable pathway beneath an impermeable glacial debris flow, a specific fluid-focussing mechanism for this area (Rajan et al. 2012). A third and very active area has been recently described by Sahling et al. (2014) on the shelf in only 90 m water depth.

Data from the area at 240 m water depth are used here to present our quantification method and strategies for gas release monitoring. Hydrographically, the area is influenced by the West Spitsbergen Current (WSC), which is a warm water branch of the North Atlantic current flowing northward together with the Coastal Current (CC), which is a continuation of the East Spitsbergen Current (ESC; Fig. 6). The CC brings less saline water into the area. Seasonal driven ice formation impacts the hydrographical changes, influencing the water stratification and thus the transport of dissolved methane through the water column.

Materials and procedures

Data acquisition and processing

The data presented here have been recorded with an EK60 scientific SBES which applies splitbeam technology; it was operated with three frequencies simultaneously (18 kHz, 38 kHz, and 120 kHz). In the following, we concentrate on the 38 kHz frequency; the beam width of this transducer is 6.7°. For data acquisition and online visualization, we used the ER60 software by Kongsberg. Post-processing is based on the FM-Midwater tool of the Fledermaus software suite (QPS) and a self-written MATLAB-based software package called FlareHunter. FlareHunter calculates target strength TS and backscattering volume strength S_V (e.g., *see* Lurton 2002) and allows three-dimensional visualization and analysis for each depth bin per ping using the mechanical angle information of the split-beam system. Ship motion compensation, static offset correction and where necessary ray-tracing needs to be carried out before further processing and interpretation can be done. This is implemented in FlareHunter.

Seep localization

Flares were identified based on the criteria presented above and manually selected in FlareHunter. The selected ping and depth interval was filtered by a user-definable threshold and cleaned manually to exclude unwanted signals from other sources (fish, plankton) and noise (seafloor multiple, other hydroacoustic systems). Seafloor signals were also excluded to derive a clean and undisturbed water column dataset. Each depth bin value of this pre-cleaned dataset was geo-referenced to receive the correct position in 3D volume. Static offsets between transducers and the GPS antenna, motion compensation (pitch, roll, yaw, and heave) were considered during post-processing (Supporting Information Appendix 1: Workflow diagram). In addition, ray tracing has been implemented in FlareHunter to consider refraction of the acoustic wave with changing sound velocity in the water column. Because of the acquired sound velocity profiles (Supporting Information Appendix 2), the water depth of only 240 m at the chosen seep area and the rather small pitch and roll angles ($< 9°$), ray tracing was deemed unnecessary to achieve a better positioning accuracy for our specific dataset.

Backscattering recorded as a flare is usually caused by multiple targets/bubbles in the acoustic beam released from localized bubble releasing vents at the seafloor. Depending on the areal extend of these vents at the seafloor and current induced spreading of bubbles while rise, bubbles in most cases fill only a small portion of the beam volume at a certain depth (Fig. 7), in shallow water wide spread bubbling can fill the beam

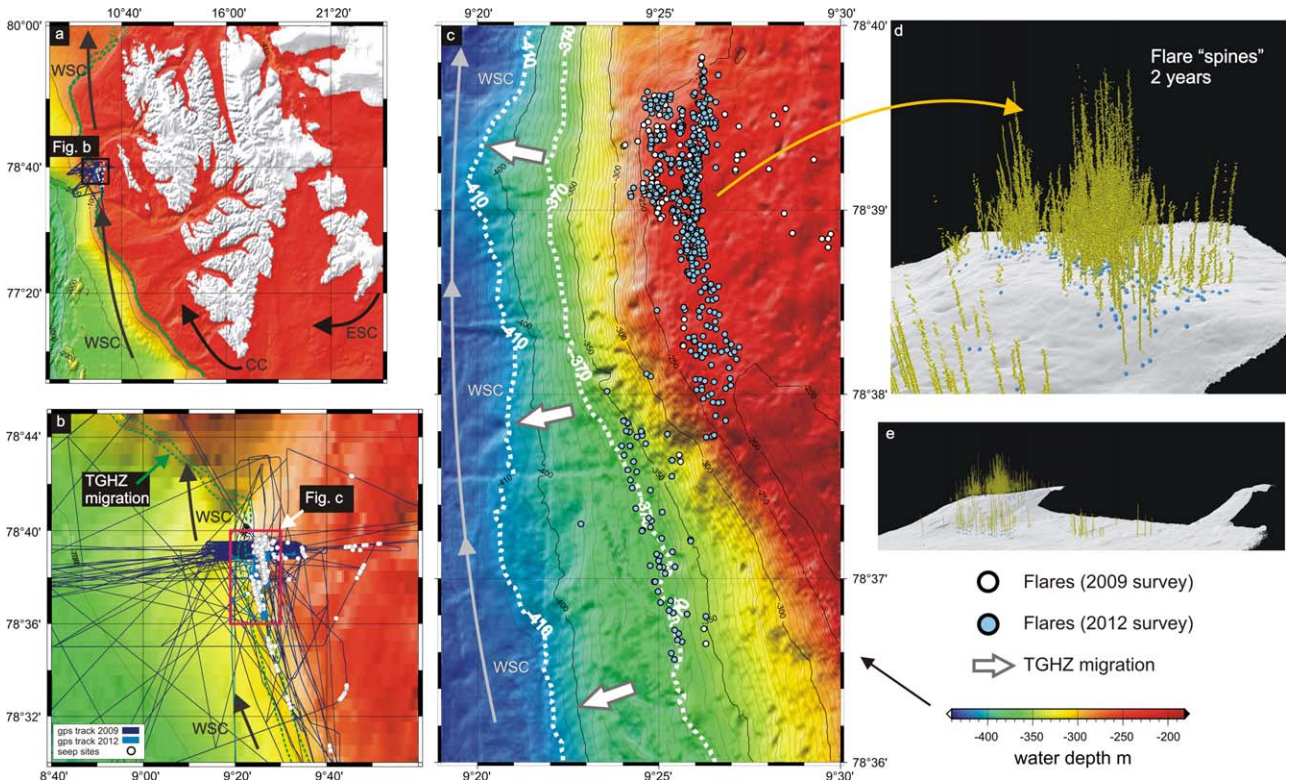

Fig. 6. (a) Bathymetric map of the Svalbard archipelago and dominating currents in the area (West Spitsbergen Current WSC; Coastal Current CC; East Spitsbergen Current ESC). (b) Track of the hydroacoustic surveys carried out in 2009 and 2012.(c) Distribution of detected seeps in the study region; yellow arrows indicate the migration of the TGHZ during the last 30 yr from 370 m down to 410 m water depth (Westbrook et al. 2009) assuming a bottom water temperature increase from 2°C to 3°C; the area densely covered with seeps at the shelf edge is the focus of our studies. Images (d) and (e) show a three-dimensional view of the "flare spines" in the study area.

completely. To better pinpoint the center of the bubble release site on the seafloor, geometric averaging was applied to the edited and position-corrected data. The geometric mean is calculated for each set of backscatter values for a certain depth range, providing a line with only one position per depth range, the "flare spine" (Fig. 7d).The lowermost point just at the seafloor can be seen as the center of the bubble release. This does not mean that each flare is the result of only one bubble vent at the seafloor, but that the center of the seep site (which most likely consists of multiple bubble vents scattered over a certain area) is the base of the flare spine.

Video footage from seep sites in the study area shows little to moderate bubble release activity of single or multiple bubble chains or clouds being released over few to tens of square meters. This means that backscattering could have been produced by single and multiple targets (bubbles) in the beam. Because the splitbeam processing of the EK60 SBES was designed to locate single targets inside the beam, bubble positioning could be faulty due to signals from multiple targets. A faulty identification of multiple targets as single target would most likely result in a random distribution, that the location of real single targets will display a certain spatial tendency. When averaging the target positions by calculating the geometric mean from several consecutive pings, it was shown that the angle information from single targets (with a spatial tendency in the beam lobe) is predominant over randomly distributed data from multiple targets (*see* Fig. 7e,f).

Inverse method for bubble volume and flow rate quantification

Accurately calculating gas flow rates using hydroacoustic methods is needed but different research groups still use very different approaches (Artemov et al. 2007; Nikolovska et al. 2008; Ostrovsky et al. 2008; Muyakshin and Sauter 2010; Jerrem et al. in press). To date, no standard methodology exists for analyzing free gas flow rates of large bubbles in deep water (>100 m) with ship-based hydroacoustic systems alone.

Gas flow rate calculations become even more complicated and uncertain if one lacks detailed information about the bubble-size distribution. The method that we introduce estimates the bubble flow rate of a group of bubble streams using the backscattering produced when insonified. The total acoustical backscattering received by the echosounder is assumed to be the contribution of single backscattering produced by several spherical bubbles of different sizes. The inversion relates the flow rate produced by the bubble

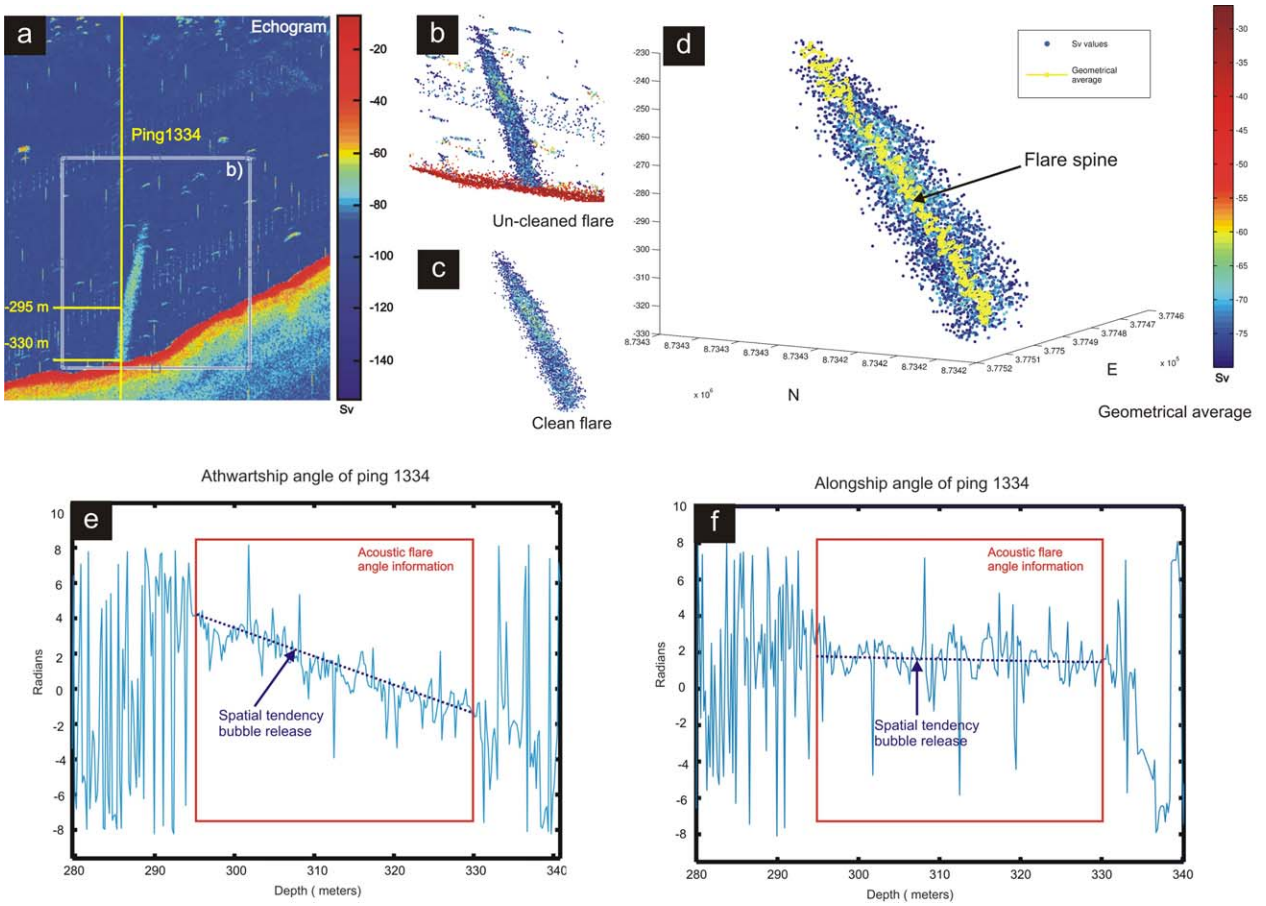

Fig. 7. Processing steps for flare analysis. (a) Identification of the acoustic flare in the echogram (38 kHz) and processing of the backscatter values inside the selected area above a specific threshold of S_V. Images (b) and (c) show the 3D visualization of the backscatter data of uncleaned and cleaned data. (d) Three-dimensional representation of the geometric mean calculated flare-spine. Images (e) and (f) represent the athwart- and alongship angle information respectively vs. the depth of one selected ping (1334) inside the flare (*see* image (a)). Data inside the red boxes are from bubble backscattering; for both angles, the more or less linear trend shows that the system correctly identifies the position of the bubbles inside the beam. Spatial uncertainties have been further decreased by calculating the geometric mean over several pings.

streams inside the beam with the differential backscattering cross-section (e.g., *see* Medwin and Clay 1988) produced by the group of bubbles. The final mathematical expression of the flow rate requires as inputs the target strength (TS) values of the acoustic flare at a predetermined depth; a probability density function of the bubble sizes that have been ideally observed at the respective seep site; BRS s; environmental properties (e.g., densities, sound speed); as well as a number of echosounder specific parameters.

Inverse method for bubble volume quantification

The insonified area of a singlebeam echosounder at the seafloor (the echosounder footprint) can cover several hundreds of square meters (a beam width of 7° covers $\sim 760\,m^2$ at 220 mbsl), and thus, the backscattering signal collected can be produced by several bubble streams (Fig. 8).

The available information obtained from the echosounder is given in terms of target strength (TS) which is the logarithmic version of the total backscattering cross-section $\Delta\sigma_{bs}$ (also known as differential backscattering cross-section, for example, *see* Medwin and Clay 1988) of the scatterers in the insonified volume (Eq. 1).

$$TS = 10 \log \Delta\sigma_{bs} \tag{1}$$

TS is calculated for each sample of each ping (e.g., Fig. 4) and therefore each TS value represents the backscattering produced by the targets located at the approximated truncated conical volume with a depth given by the time sample interval of the received signal (sample volume V; Fig. 8).

If multiscattering effects are neglected, the total backscattering cross-section of the sample volume can be simply assumed as the summation of single backscattering cross-sections produced by the scatterers within the sample volume V. If the scatterers are considered to be bubbles with different sizes, the total backscattering cross-section coming from a sample volume is given by

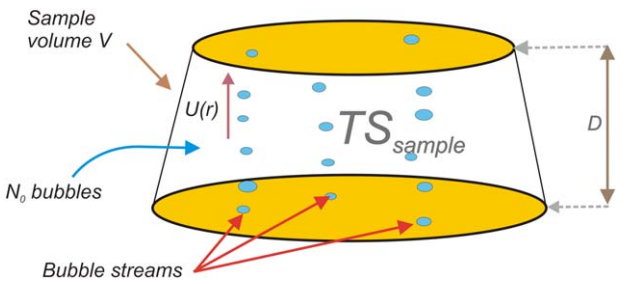

Fig. 8. Illustration of bubble streams covered by the sample volume V of the echosounder at a specific depth. Here, N_0 represents the total number of bubbles inside the sample volume V; TS_{sample} represents the target strength of the sample volume V; $U(r)$ is the BRS as function of the bubble size; and D the height of the sample volume V.

$$\Delta\sigma_{bs}=N_1\sigma_{bs1}+N_2\sigma_{bs2}+\ldots N_n\sigma_{bsn}=\sum_{i}^{n}N_i\sigma_{bsi} \tag{2}$$

where σ_{bsi} represents the backscattering cross-section of a single bubble of i-size and N_i the number of bubbles of i-size inside the sample volume.

The equivalent of Eq. 2 in the continuous domain can be expressed as

$$\Delta\sigma_{bs}=\int_{r_1}^{r_2}N(r)\sigma_{bs}(r)dr \tag{3}$$

where,

$$N_0=\int_{r_1}^{r_2}N(r)dr \tag{4}$$

N_0: Total number of bubbles inside the sample volume V
$N(r)$: Distribution of bubbles in function of the radius size [1/m]
r_1, r_2: Lower and upper limit of the bubble-size distribution

In Eq. 3,σ_{bs} represents the theoretical backscattering cross-section of a single bubble. In this work, we use the equation given by Thuraisingham (1997; Fig. 9a) to calculate σ_{bs} as this expression is valid for all kr values, where k represents the wave number, and r the bubble radius (5).

$$\sigma_{bs}=\frac{r^2}{\left[\left(\left(\frac{r_0}{r}\right)^2-1\right)^2+\delta(r,f_{\text{echo}})^2\right]}\frac{(\sin kr/kr)^2}{1+(kr)^2} \tag{5}$$

where,

r_0: Bubble resonant radius at echosounder frequency and specific static pressure [m]
k: Wave number $\left(\frac{2\pi f_{echo}}{c}\right)$
f_{echo}: Echosounder frequency [Hz]
δ: Dimensionless damping

Expressions for the damping δ (Ainslie 2010) and the resonance frequency ω_M (Minnaert 1933) valid for moderately large bubbles (radius exceeding 100 μm), are presented in Eqs. 6 and 7a–7c and 8, respectively (Supporting Information Appendix 3).

$$\delta(r,\omega)=\delta_{\text{rad}}+\delta_{\text{therm}}+\delta_{\text{visc}} \tag{6}$$

$$\delta_{\text{rad}}=\omega_{\text{M}}r/c_{\text{w}} \tag{7a}$$

$$\delta_{\text{therm}}=\frac{3(\gamma-1)}{r}\left(\frac{D_a}{2\omega_{\text{M}}}\right)^{\frac{1}{2}} \tag{7b}$$

$$\delta_{\text{visc}}=\frac{(\eta_{\text{S}}+3\eta_{\text{B}})}{\rho_{\text{W}}\omega_{\text{M}}r^2} \tag{7c}$$

$$\omega_{\text{M}}=\left(\frac{3\gamma P_{\text{st}}}{\rho_W r^2}\right)^{\frac{1}{2}} \tag{8}$$

where,

δ_{rad}: Re-radiation damping term (dimensionless)
δ_{therm}: Thermal damping term (dimensionless)
δ_{visc}: Viscous damping term (dimensionless)
ω_{M}: Minnaert frequency [rad/s]
c_{w}: Speed of sound in the seawater [m/s]
γ: Specific heat ratio of gas (dimensionless)
D_a: Thermal diffusivity [m^2/s]
η_{S}: Shear viscosity [Pa][s]
η_{B}: Bulk viscosity [Pa][s]
ρ_{W}: Water density [kg/m^3]
P_{st}: Static pressure [Pa]

The value of r_0 in (5) was calculated using the breathing frequency expression (9) developed by Minnaert (Minnaert 1933; Medwin and Clay 1998). Figure 10b depicts r_0 values at different depths for a 38 kHz frequency,

$$r_0=\frac{1}{2\pi f_{\text{ECHO}}}\left(\frac{3\gamma P_{\text{st}}}{\rho_{\text{W}}}\right)^{\frac{1}{2}} \tag{9}$$

where,

γ: Specific heat ratio of gas (dimensionless)
ρ_{W}: Water density [kg/m^3]
f_{ECHO}: Echosounder frequency [Hz]
P_{st}: Static pressure [Pa]

As stated above, singlebeam echosounders can cover an area with several bubble streams. Therefore, the mathematical expression of the total flow rate linked to the obtained acoustical backscattering must represent the backscattering produced by these several bubble streams. If it is assumed that all the bubbles released are approximately spherical the

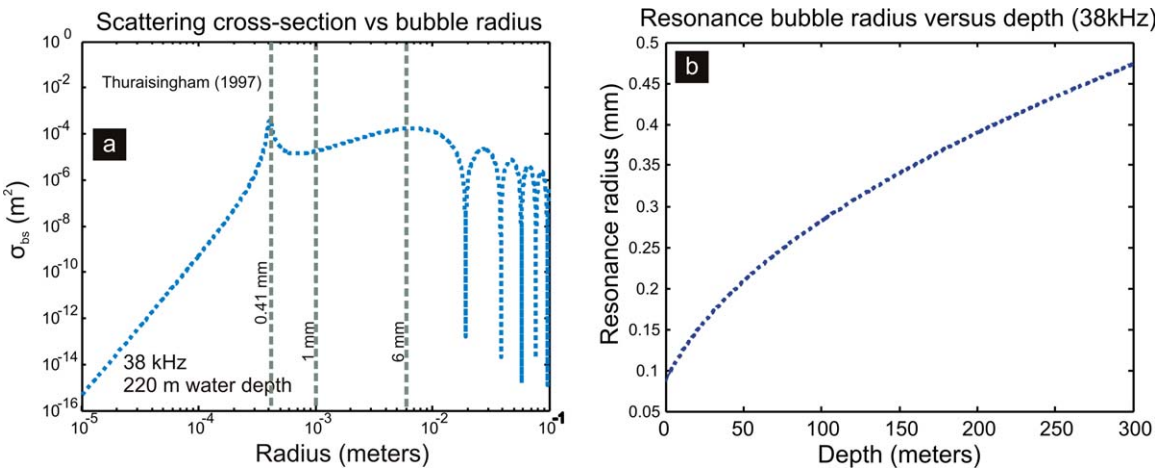

Fig. 9. (a) Acoustic backscattering cross section σ_{bs} as function of the bubble radius using the mathematical expressions of Thuraisingham (1997) for a single bubble, considering bubbles at 220 m and using the Minnaert frequency (Minnaert 1933) as resonance frequency. (b) Representation of the Minneart resonance radius at different depths for a pure methane bubble insonified with 38 kHz.

volumetric bubble flow rate of a group of bubble streams can be defined as following,

$$\varnothing_{\mathrm{V}} = \frac{4\pi}{3}\sum_{i}^{n} r_i^3 N_i/\Delta t_i \tag{10}$$

And its equivalent mass bubble flow rate as,

$$\varnothing_{\mathrm{M}} = \rho_{\mathrm{G}}\frac{4\pi}{3}\sum_{i}^{n} r_i^3 N_i/\Delta t_i \tag{11}$$

where,

r_i: Bubble radius of i-size [m]
N_i: Number of bubbles of i-size inside the volume sample V
Δt_i: Time necessary to fill the volume sample V with N_i bubbles of r_i radius [sec]
ρ_{G}: Gas density of the bubble at the respective water depth [kg/m^3]

To relate the flow rate with the volume sample (Fig. 8), we assume that the time Δt_i is necessary to fill the volume sample V with N_i bubbles of r_i radius. If we consider U_i as the average BRS of a bubble of r_i radius and D the vertical distance that the bubble needs to travel from the lower to the upper limit of the sample volume V, the massive flow rate (Eq. 11) can be replaced by,

$$\varnothing_{\mathrm{M}} = \rho_{\mathrm{G}}\frac{4\pi}{3D}\sum_{i}^{n} r_i^3 N_i U_i \tag{12}$$

where,

U_i: Average BRS of i-size bubble (m/sec)
D: Height of volume sample [m]

The equivalent expression of Eq. 11 in the continuous domain can be expressed as following,

$$\varnothing_{\mathrm{M}} = \rho_{\mathrm{G}}\frac{4\pi}{3D}\int_{r_1}^{r_2} r^3 N(r)U(r)dr \tag{13}$$

where,

$U(r)$: BRS in function of the bubble radius [m/sec]

To obtain our inverted expression of the total mass flow rate $\varnothing_{\mathrm{M}}$ related to the backscattering $\Delta\sigma_{bs}$ coming from the sample volume V, Eqs. 3 and 13 are combined. The total mass flow rate of the bubble streams inside the sample volume is then given by

$$\varnothing_{\mathrm{M}} = \rho_{\mathrm{G}}\Delta\sigma_{bs}\frac{4\pi}{3D}\frac{\int_{r_1}^{r_2} r^3 N(r)U(r)dr}{\int_{r_1}^{r_2} N(r)\sigma_{bs}(r)dr} \tag{13a}$$

or its equivalent using the TS value (Eq. 1)

$$\varnothing_{\mathrm{M}} = \rho_{\mathrm{G}}10^{\frac{\mathrm{TS}}{10}}\frac{4\pi}{3D}\frac{\int_{r_1}^{r_2} r^3 N(r)U(r)dr}{\int_{r_1}^{r_2} N(r)\sigma_{bs}(r)dr} \tag{13b}$$

Lets assume that the distribution of bubbles $N(r)$ inside the volume sample is equal to the total number of bubbles N_0 multiplied by the probability density function $f(r)$ of the bubble-size distribution. As we further know that D

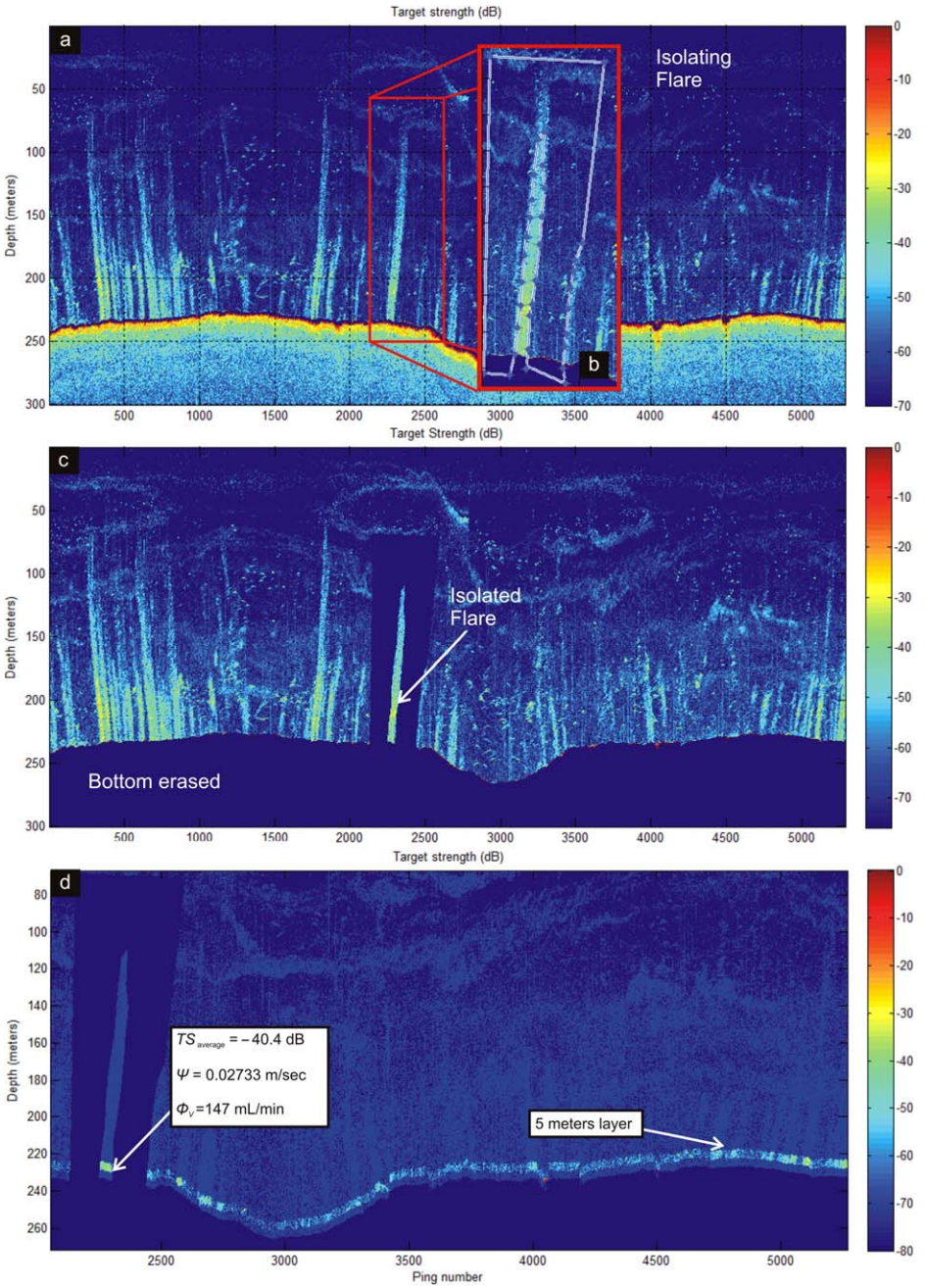

Fig. 10. Acoustic flare detection and flow rate estimation processing using FlareHunter GUI; (a) TS echogram (beam compensated) filtered with a lower threshold of −70 dB; (b) Removal of "noise" surrounding an isolate flare; (c) Isolated flare with removed signals from the seafloor and below; (d) Layer selection to calculate $\overline{TS}$ at near the seafloor of the flare. The figure shows Ψ value and the estimated flow rate using the Leifer model for clean bubbles to estimate BRS.

represents the depth of the volume sample which can also be expressed as a function of the sample interval τ and the sound propagation speed c_w in the water., Eq. 13 can be rewritten as:

$$\varnothing_M = \rho_G 10^{\frac{TS}{10}} \Psi \tag{14}$$

where,

$$\Psi = \frac{8\pi}{3 c_w \tau} \frac{\int_{r_1}^{r_2} r^3 f(r) U(r) dr}{\int_{r_1}^{r_2} f(r) \sigma_{bs}(r) dr} \tag{15}$$

$f(r)$: Probability density function of the bubble-size distribution [1/m]

τ: Sample interval [sec]

Flow rate quantification

TS average values were extracted from flares visualized in echograms using FlareHunter. All TS values in echograms were compensated for their position in the beam using the Simrad split-beam method described by Echoview (Echoview webpage: http://www.echoview.com/).

Acoustic flares were identified within the TS echograms and TS average values ($\overline{TS}$) of each flare at the source near the seafloor were stored together with additional information as, for example, water depth, footprint at the specific depth, geographic coordinates, or sound speed. To decrease the effect of background noise, data below −70 dB were threshold filter for the entire echogram (Fig. 10a). To isolate single flares, the backscattering surrounding the flare was manually removed (Fig. 10b,c). Backscattering coming clearly from fish (shape with stronger signal than the flare) was manually removed (edited in 3D using MATLAB functionality) to avoid overestimation of flow rates. To evaluate the flow rate of the flares, the TS values coming from a five meter thick layer with the lower boundary 5 m above the seafloor were used (Fig. 10d). TS values coming from this layer of a single flare were geometrically averaged to obtain one representative $\overline{TS}$ value for the strength of bubble release close to the source at the seafloor. We choose this layer from 5 m to 10 m above the bottom to be as close as possible to the source (and with as little as possible changes in bubble size due to bubble dissolution while rise) but avoiding reverberation effects of the signals at the seafloor. The $\overline{TS}$ value was calculated using the following mathematical equation,

$$\overline{TS} = 10 \log\left(\left[\prod_{i=1}^{n_P} 10^{\frac{TS_i}{10}}\right]^{\frac{1}{n_P}}\right) \quad (16)$$

where,

TS_i: Target strength of different samples inside the selected layer [dB]

n_P: Number of samples

The final flow rate (mass and volumetric) of each of the detected acoustic flares was estimated using Eq. 14.

As defined in Eq. 14, the parameter Ψ depends on $f(r)$, $U(r)$, r_0, and δ. The probability density function $f(r)$ was calculated from a polynomial fit of visual bubble-size measurements carried out in 2011 and 2012 (McGovern 2012; solid green line in Fig. 11).

$U(r)$ was calculated for bubbles of 1 mm to 6 mm in diameter using a MATLAB-based script kindly provided by Ira Leifer (Fig. 12; Bubbleology Research International). This script considers bubble rise models of Mendelson (1967), Woolf and Thorpe (1991),Woolf (1993), Leifer et al. (2000), and Leifer and Patro (2002).

Temperature and salinity are necessary input parameters in those models. Based on CTD profiles, we used 4°C and a salinity of 35 PSU at 220 m water depth (*see* profiles Supporting Information Appendix 1). Radii r_0 for each flare were estimated using the corresponding average layer depth following Eq. 9. The damping δ and Minnaert frequency ω_M were calculated for bubble sizes between 1 mm and 6 mm using Eqs. 6, 7, and 8, and the needed constants detailed in Table 1. The gas density ρ_G at different water depth for pure methane was calculated using the simplified equation given by (Medwin and Clay 1988, with a atmospheric density of methane ρ_{G0} of 0.66 kg/m^3 ρ_{G0}.

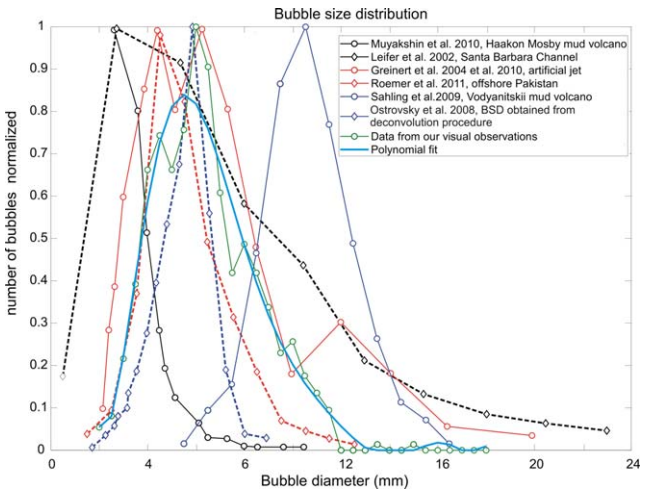

Fig. 11. BSD from our video observations (green line with circles) in comparison to other published data. For our gas flow rate estimation, we considered bubbles with a radius from 1 mm to 6 mm; none of them is resonant in 220 m water depth (Fig. 9b).

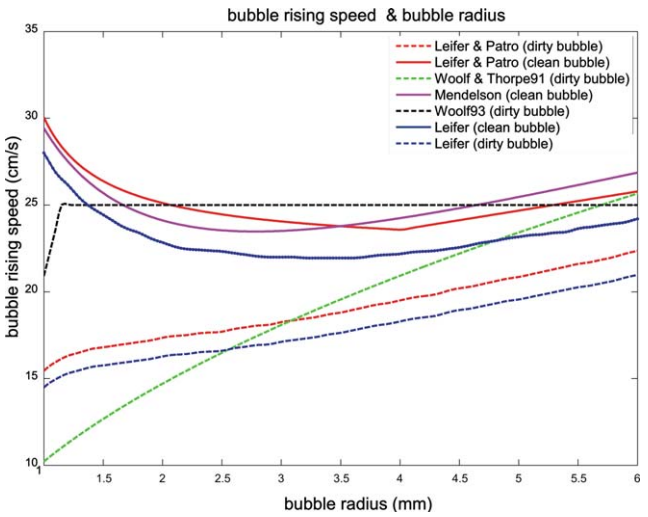

Fig. 12. Representation of the BRS as function of the bubble radius (1 mm to 6 mm) using different published models (Mendelson 1967; Woolf and Thorpe 1991;Woolf 1993; Leifer et al. 2000; Leifer and Patro 2002).

Table 1. Constants values used to evaluate flow rates of each acoustic flare

Constant	Symbol	Value
Atmospheric CH_4 density	ρ_{G0}	0.66 [kg/m^3]
Surface tension water	σ	0.074 [N/m]
Most frequent bubble radius BSD	r_{av}	0.003 [m]
Average sound velocity seawater	c_w	1467 [m/s] (from sound speed profiles, Supporting Information Appendix 1)
Specific heat ratio of gas	γ	1.4
Thermal diffusivity	D_a	9.19 e − 7 [m^2/s^{-1}]
Shear viscosity	η_S	1.519 e − 3 [Pa/s]
Bulk viscosity	η_B	$2.2\eta_S$ [Pa/s]
Water density	ρ_W	1028 [kg/m^2] (derived from CTD casts)
Echosounder frequency	f_{ECHO}	38,000 [Hz]
Atmospheric pressure	P_{st0}	101,325 [Pa]
Acceleration of gravity	g	9.8 [m/s^2]
Static pressure at bubble depth	P_{st}	$P_{st0} + \rho_W g Z$ [Pa]
Water depth of bubbles	Z	Average depth of layer at each acoustic flare
Average temperature	T	4°C (used in BRS models; from temperature profiles, Supporting Information Appendix 1)
Salinity	S	35 PSU (used in BRS models; from salinity profiles, Supporting Information Appendix 1)

$$\rho_G = \rho_{G0}\left(1+\frac{2\sigma}{P_{st}r_{av}}\right)(1+0.1Z) \quad (17)$$

where,

ρ_{G0}: Atmospheric CH_4 density

σ: Surface tension water [N/m]

r_{av}: Most frequent bubble radius bubble-size distribution (BSD) [m]

Z: Average depth of layer at each acoustic flare

A more precise density can be calculated using the SUGAR toolbox by Kossel et al. (2013).

To assign an average flow rate to a cluster of flares forming a seep site, flares were clustered if the footprints overlap (Fig. 13). Once the clustering is done, the average bubble flux $\Omega^C_{M,V}$ (volumetric or in mass) can be obtained using the following expression,

$$\Omega^C_{M,V} = \frac{1}{p}\left(\frac{\varnothing^1_{M,V}}{A_1}+\frac{\varnothing^2_{M,V}}{A_2}+\frac{\varnothing^3_{M,V}}{A_3}+\cdots+\frac{\varnothing^P_{M,V}}{A_p}\right)=\frac{1}{p}\sum_i^p\frac{\varnothing^i_{M,V}}{A_i} \quad (18)$$

where,

$\varnothing^i_{M,V}$: Flow rate (volumetric or in mass) of an i-acoustic flare [m^3/s or kg/s]

A_i: Area of echosounder footprint of the source of an i-acoustic flare [m^2]

p: Number of acoustic flares that belong to the cluster

To evaluate the average flow rate of each cluster $\varnothing^C_{M,V}$, the average bubble flux $\Omega^C_{M,V}$ is multiplied by the area of the cluster A_C (Fig. 13c). The cluster area was calculated by gridding all footprints (Fig. 13c). The cluster flow rate $\varnothing^C_{M,V}$ was then calculated as:

$$\varnothing^C_{M,V} = \Omega^C_{M,V}A_C = \Omega^C_{M,V}N_{Cells}\Delta x\Delta y \quad (19)$$

where,

A_C: Cluster area [m^2]

N_{Cells}: Number of cells inside the cluster area

$\Delta x, \Delta y$: cell size in x and y direction (here related to UTM coordinates) [m]

Finally, the estimation of the total flow rate $\varnothing^T_{M,V}$ of the study area is done by adding the flow rates of the each cluster and isolated flares (flares without overlapping footprints).

$$\varnothing^T_{M,V} = \sum_i \varnothing^{C,i}_{M,V} \quad (20)$$

where,

$\varnothing^{C,i}_{M,V}$: Flow rate of i-cluster or i-isolated flare

Assessment

Methane flow rates and fluxes offshore PKF

During the surveys in 2009 and 2012, the same seep area was investigated. Unfortunately, we could not rerun the same survey lines because of time limitations; the very dense EW line spacing in 2009 was part of a 3D-seismic survey. However, two slightly oblique surveys covered the main seep area in 2012; slight differences in coverage remain. Figure 14 presents the final acoustic maps from both years of SBES mapping as well as a map where both surveys are merged (Fig. 14d).

Final flow rates and flux estimates (per volume and mass) per minute and extrapolated to one-year are shown in Table 2. They are based on the above mentioned inverse method to calculate. $\varnothing^T_{M,V}$ using the Thuraisingham model of acoustical backscattering cross-section of bubbles and applying

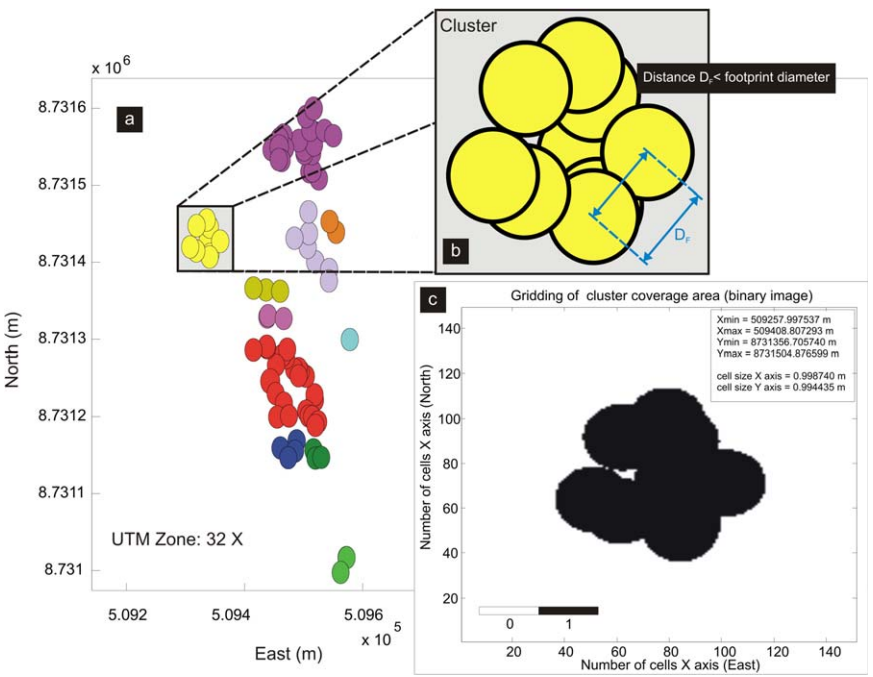

Fig. 13. Example of the clustering process of detected flares; (a) Several clusters in the study area (different colors); sizes of circles are equivalent to the footprint of the echosounder at the layer average depth; (b) Zoom in of one cluster example showing the overlap of the footprint; (c) combination of the overlapping footprints to estimate the cluster area.

different models for calculating BRS. We chose to present flow rates for a one-year period to provide data in the same unit as other authors (Judd et al. 1997; Hornafius et al. 1999; Sauter et al. 2006). We think that extrapolating flow rates to "one year" based on short-term one-day observations needs to be treated carefully as they most likely are not a valid representation for the entire year. However, repeated flow rate measurements of one-day or maybe one-hour period provide important information about short time flow variability.

In addition to the uncertainty described in Table 2, another uncertainty derives from the bubble-size distribution; it is necessary to accurately measure BSD to obtain realistic values of the flow rate. Table 3 shows an example of the differences in flow rate values based on different published BSD (Ostrovsky et al. 2008; Sahling et al. 2009; Römer et al. 2011). In addition, the BSD from McGovern (2012) and a uniform bubble size of 6 mm in diameter were used. We used an example flare and the average TS value at the source near the bottom (Fig. 15) to calculate flow rates. Uncertainties are given in Table 3, with 60% of relative error the BSD is more important than rising speed and uncertainties in the absolute TS value.

Discussion

The following discussion only deals with the presented methodology. We do not attempt to discuss or even answer the observed changes in fluxes between the two survey years. This will be part of another study where we compare fluxes from yearly surveys between 2008 and 2014 over the same area presented here.

Limitations of the methodology

Methods quantifying free gas flow rates in lakes and oceans using hydroacoustic measurements have recently undergone a series of developments that improved their reliability and accuracy. This is particularly true for shallow-water studies, for example, in lakes as described by Ostrovsky et al. (2008) and DelSontro et al. (2011). In deep water (> 100 m), methodologies link visual observations and direct flow rate measurements (e.g., inverted funnels) with the larger-scale occurrence of seeps observed in single- or multibeam data (Nikolovska et al. 2008; Greinert et al. 2010; Römer et al. 2012b). Not always are links between the hydroacoustic backscatter intensity and direct flow rate measurements established. This could result in an empirical relationships that allows better extrapolations if applied to the measured acoustic data. Although the flow rate estimates presented still need to be validated using either discrete measurements, visual or high-frequency acoustic measurements by remotely operated vehicle (ROV) deployments, we are confident that our flux estimates are reasonable and representative for the area at the time of the survey in July 2009 and 2012.

Our approach follows the understanding that the received acoustic signal is generated by the contribution of the backscattering produced by several single targets (Artemov 2006;

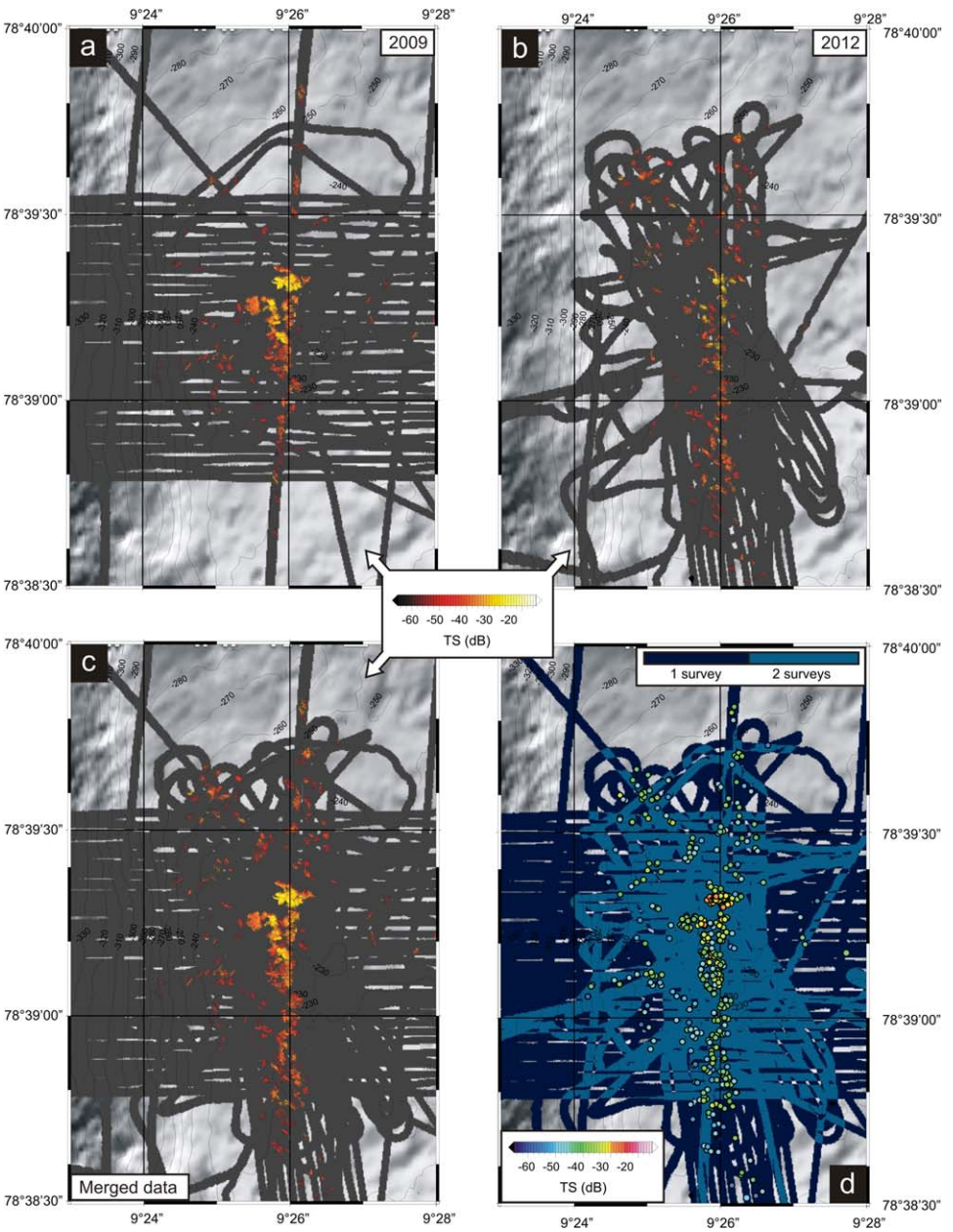

Fig. 14. (a,b) Acoustic maps of bubble induced backscattering (TS values) above the seafloor. (c) Map of merged backscattering TS over 2 yr. Gray areas in images (a) to (c) indicate the insonified area/footprint. (d) Overlap of the insonified areas in 2009 and 2012. Areas covered once are dark blue; those covered twice are lighter blue. Colored circles represent target strength at the center of the footprint in the selected depth layer.

Muyakshin and Sauter 2010; Weber et al. 2014). As mentioned earlier, we use a set of assumptions on which our method is based. We assume that (a) the targets are spherical bubbles of different sizes, each one being an isotropic scatterer. As the scattering of a single bubble can be related to its radius and, therefore, its volume (Wildt 1946), it is (b) also assumed that the scattering generated by multiple bubbles is related to the total volume of the bubbles within the insonified volume of water (Medwin 1977). We are aware that assumptions (a) and (b) may have a large uncertainty because they "idealize" real conditions and a purely summation of the backscattered energy coming from single targets has limited application validity. To our knowledge, there is no finally validated and conclusive backscatter model for large wobbly bubbles or bubble clouds insonified with low frequency echosounders in water depth > 100 m where multiple backscattering (backscattering of energy that does not directly come from the transducer but from other bubbles, but which is also received by the transducer) might occur as well. Advanced models that describe the backscattering strength of large, none spherical

Table 2. CH_4 flow rates and fluxes with respect to different BRS models (Mendelson 1967; Woolf and Thorpe 1991; Woolf 1993; Leifer et al. 2000; Leifer and Patro 2002). The table also includes the mean, standard deviation, relative error using the different BRS models, and the relative error produced by ± 1 dB of variation in the TS value of the source of the acoustic flare

Data period	2009		2012		2 yr merged	
			Total covered area (m^2)			
	101,285.61		158,632.36		231,930.41	
BRS model						
Clean bubbles	$\varnothing_V^T$ (L/min)	$\varnothing_M^T$ (T/yr)	$\varnothing_V^T$ (L/min)	$\varnothing_M^T$ (T/yr)	$\varnothing_V^T$ (L/min)	$\varnothing_M^T$ (T/yr)
Leifer "clean bubble" (mean=0.231 m/s)	36.58	300.48	42.83	354.38	64.76	534.50
Mendelson "clean bubble" (mean=0.249 m/s)	46.18	379.26	54.06	447.29	81.75	674.63
Leifer& Patro "clean bubble" (mean=0.249 m/s)	45.61	374.65	53.40	441.86	80.76	666.43
Mean	42.79	351.46	50.09	414.51	75.75	625.18
Standard deviation	5.38	44.21	6.30	52.14	9.53	78.64
Relative error, BRS models (%)			± 14.53			
Approximated relative error, ±1dB TS value (%)			± 26.40			
			Mean Flux ($1000\times\varnothing_{M,V}^T/m^2$)			
	0.42	3.47	0.32	2.61	0.33	2.70
Dirty bubbles	$\varnothing_V^T$ (L/min)	$\varnothing_M^T$ (T/yr)	$\varnothing_V^T$ (L/min)	$\varnothing_M^T$ (T/yr)	$\varnothing_V^T$ (L/min)	$\varnothing_M^T$ (T/yr)
Leifer & Patro "dirty bubble" (mean=0.190 m/s)	37.04	304.19	43.36	358.76	65.57	541.11
Woolf & Thorpe "dirty bubble" (mean=0.191 m/s)	39.79	326.79	46.58	385.41	70.44	581.29
Woolf 93"dirty bubble" (mean=0.249 m/s)	46.23	379.68	54.12	447.79	81.84	675.37
Leifer "dirty bubble" (mean=0.178 m/s)	30.15	247.60	35.29	292.02	53.37	440.44
Mean	38.30	314.56	44.83	370.99	67.80	559.55
Standard deviation	6.66	54.71	7.80	64.52	11.79	97.32
Relative error, BRS models (%)			± 17.39			
Approximated relative error, ± 1dB TS value (%)			± 26.40			
			Mean Flux ($1000\times\varnothing_{M,V}^T/m^2$)			
	0.38	3.11	0.28	2.34	0.29	2.41

and wobbly bubbles that travel in close distance to each other could easily be included in our methodology by replacing Eqs. 6 to 9. Despite the used simplification and the existing uncertainties about BSD and BRS, our results give reasonable approximations for methane flow rates that are in agreement with direct observations (McGovern 2012; Sahling et al. 2014).

Uncertainties of bubble size and rising speed

Many optical observations at seep sites of different release intensities and in different water depths show that bubbles of 1 mm to 12 mm in diameter present the most common sizes with a mean diameter of 6 mm that is frequently found (*see* references in Fig. 11). Larger bubbles are neither spheres nor ellipsoids but represent rather irregularly shaped oblate forms that change shape while rising in a wobbly fashion (Ostrovsky et al. 2008; Leifer and Culling 2010). The shape of the bubble depends on the forces acting on it and only below a certain size where the surface tension force predominates do bubbles become spherical (Bhaga and Weber 1981); the same is true for larger bubbles if they are gas-hydrate skinned (Rehder et al. 2009).

Flow rate estimates obviously strongly depend on the (BSD) and the BRS. For our flow rates and flux calculations, the BSD obtained from our optical data was considered to be representative for the release within the study area although only 17 seep locations scattered over the entire area were observed for a very short time and only 641 bubbles in total have been analyzed (McGovern 2012). The BSD as well as the mean bubble size agree well with results from similar seep settings (*see* references in Fig. 11). Nevertheless, more detailed visual observations are needed to assess the spatial and temporal variability of the BSD in the area to decrease uncertainties in our flow rate calculations. BSD estimates without visual verification leave uncertainties that ideally could be reduced. However, detailed measurements need large and expensive equipment as ROVs and cannot always be conducted. We think that such uncertainties should be clearly stated in any publication.

The final flow rate estimate is very sensitive to BRSs (*see* Table 2). BRSs are ideally obtained directly from optical or hydroacoustic measurements. We used BRSs from various models (*see* references in Fig. 12) that have been verified by direct observations. However, until the BRS has been measured in the field, it remains uncertain if bubbles are "dirty" or "clean" or something in between. Environmental conditions, for example, ocean currents are equally important to

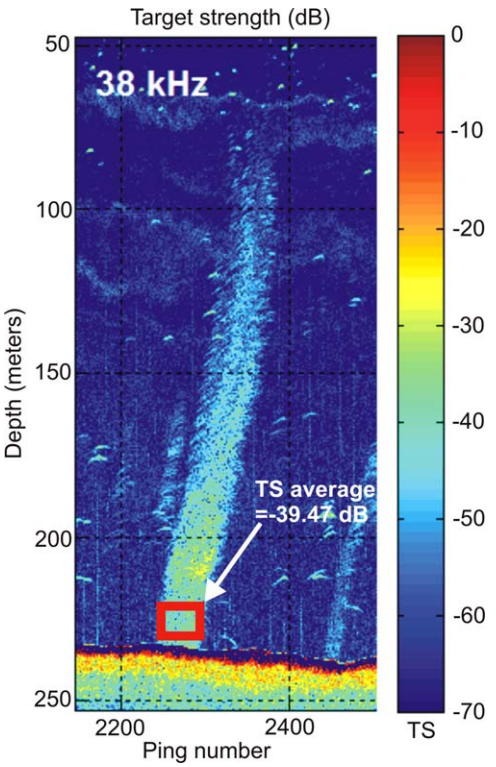

Fig. 15. Acoustic flare used to evaluate the flow rate at the source using different BSD.

Table 3. Estimation of flow rates using different BSD

BSD	Flow rate (mL/sec)
BSD from our visual observations (McGovern 2012)	181.02
All bubbles same size (diameter:6mm, most frequent value of our BSD)	110.38
BSD from Ostrovsky et al. (2008)	108.42
BSD from Sahling et al. (2009)	412.61
BSD from Römer et al. (2011)	136.52
Mean	189.79
Standard deviation	127.95
Relative error (%)	± 60.30

measure. Bubble release intensity driven by plume dynamics (bubbles inducing upwelling of water) and thus faster rising speeds need to be considered as well. For our data, final flow rates show up to 53% difference between the used BRSs (Table 2).

Backscatter and resonance of bubbles and bubble clouds

We would like to emphasize the importance of choosing the best model for calculating the backscattering cross-section of natural bubbles. We are aware that our approach in calculating the free gas flow rate is idealized as we assume large, spherical bubbles. It is known that large bubbles deform while rising and assuming an isotropic radiation of the incoming pressure wave adds to the uncertainties. According to literature, rising bubbles can be classified into three main types based on their shape after reaching the terminal velocity: the spherical, ellipsoidal, and spherical-cap types (Amaya-Bower and Lee 2010). The bubbles in our working area belong to the ellipsoidal type (oblate bubbles, 2 mm to 12 mm in diameter; BRS (Leifer model; clean bubble) 0.19–0.24 [m/sec]; Weber number 1.05–9.77 [dimensionless]); this shape is mainly determined by surface tension. Several theoretical studies give other models/equations to calculate the scattering cross-section and resonance values of nonspherical, especially oblate, bubbles (Strasberg 1953; Stanton 1989; Feuillade and Werby 1994; Leblond et al. 2014). These can be included in future calculations to improve the accuracy of flow rate estimates with our given approach (replacing Eq. 5).

In this study, we considered a scattering cross-section model for spherical bubbles that is based on the monopole bubble theory. The model developed by Thuraisingham (1997) is valid for all *kr* values. The Thuraisingham model might be more appropriate than that of, for example, Wildt (1946), but it has not been validated for both greater water depths and natural conditions where several bubbles might be very close to each other with clean or dirty surfaces. Multiple scattering effects (Foldy 1945; Carey and Roy 1993; Prosperetti et al. 1993) and the generation of a bubble-cloud specific resonance frequency have not been taken into account either, although this might have unforeseen implications.

Apart from these mostly theoretical problems, it remains unclear how the final backscattering could be recorded with state-of-the-art SBES and MBES under natural conditions. Direct flow rate validations in the field would provide answers to some of the questions related to the present simplifications in calculating the scattering cross-section. However, our results show reasonable flow rate values. Improvements could be done by either very accurately observing the shape and behavior of natural bubbles by optical means or by producing bubbles artificially at the seafloor, exactly knowing the BRS and bubble shape from lab experiments (visual confirmation should be also given). The results of such studies would certainly enhance the accuracy of ship-based free gas flow rate quantifications and would help to find a widely accepted model to estimate free gas flow rates and fluxes from the ocean floor through the water column from both deep and shallow water.

References

Ainslie, M. A. 2010. Principles of sonar performance modeling. Springer.

Amaya-Bower, L., and T. Lee. 2010. Single bubble rising dynamics for moderate Reynolds number using lattice Boltzmann method. Comput. Fluids **39**: 1191–1207. doi: 10.1016/j.compfluid.2010.03.003

Archer, D., B. Buffett, and V. Brovkin. 2009. Ocean methane hydrates as a slow tipping point in the global carbon cycle. Proc. Natl. Acad. Sci. USA **106**: 20596–20601. doi:10.1073/pnas.0800885105

Artemov, Y. G. 2006. Software support for investigation of natural methane seeps by hydroacoustic method. Mar. Ecol. J. **5**: 57–71.

Artemov, Y. G., V. Egorov, G. Polikarpov, and S. Gulin. 2007. Methane emission to the hydro-and atmosphere by gas bubble streams in the Dnieper paleo-delta, the Black Sea. Mar. Ecol. J. **3**: 5–26. doi:10.0.0.194:8080/dspace/handle/99011/622

Berndt, C., and others. 2014. Temporal constraints on hydrate-controlled methane seepage off Svalbard. Science **343**: 284–287. doi:10.1126/science.1246298

Bhaga, D., and M. Weber. 1981. Bubbles in viscous liquids: Shapes, wakes and velocities. J. Fluid Mech. **105**: 61–85. doi:10.1017/S002211208100311X

Biastoch, A., and others. 2011. Rising Arctic Ocean temperatures cause gas hydrate destabilization and ocean acidification. Geophys. Res. Lett. **38**: L08602. doi:10.1029/2011GL047222

Carey, W. M., and R. A. Roy. 1993. Sound scattering from microbubble distributions near the sea surface. In Ocean reverberation (p. 25–43). Springer Netherlands.

Chand, S., and others. 2012. Multiple episodes of fluid flow in the SW Barents Sea (Loppa High) evidenced by gas flares, pockmarks and gas hydrate accumulation. Earth Planet. Sci. Lett. **331–332**: 305–314. doi:10.1016/j.epsl.2012.03.021

DelSontro, T., M. J. Kunz, T. Kempter, A. Wüest, B. Wehrli, and D. B. Senn. 2011. Spatial Heterogeneity of Methane Ebullition in a Large Tropical Reservoir. Environ. Sci. Technol. **45**: 9866–9873. doi:10.1021/es2005545

Feuillade, C., and M. F. Werby. 1994. Resonances of deformed gas bubbles in liquids. J. Acoust. Soc. Am. **96**: 3684–3692. doi:10.1121/1.410558

Foldy, L. L. 1945. The multiple scattering of waves. Phys. Rev. **67**: 107–119. doi:10.1103/PhysRev.67.107

Granin, N. G., S. Muyakshin, M. Makarov, K. Kucher, I. Aslamov, L. Granina, and I. Mizandrontsev. 2012. Estimation of methane fluxes from bottom sediments of Lake Baikal. Geo-Mar. Lett. **32**: 427–436. doi:10.1007/s00367-012-0299-6

Greinert, J., Y. Artemov, V. Egorov, M. De Batist, and D. Mcginnis. 2006. 1300-m-high rising bubbles from mud volcanoes at 2080 m in the Black Sea: Hydroacoustic characteristics and temporal variability. Earth Planet. Sci. Lett. **244**: 1–15. doi:10.1016/j.epsl.2006.02.11

Greinert, J., D. F. Mcginnis, L. Naudts, P. Linke, and M. De Batist. 2010. Atmospheric methane flux from bubbling seeps: Spatially extrapolated quantification from a Black Sea shelf area. J. Geophys. Res: Oceans **115**: C01002. doi:10.1029/2009JC005381

Heeschen, K. U., A. M. Tréhu, R. W. Collier, E. Suess, and G. Rehder. 2003. Distribution and height of methane bubble plumes on the Cascadia Margin characterized by acoustic imaging. Geophys. Res. Lett. **30**: 12. doi:10.1029/2003GL016974

Hornafius, J. S., D. Quigley, and B. P. Luyendyk. 1999. The world's most spectacular marine hydrocarbon seeps (Coal Oil Point, Santa Barbara Channel, California): Quantification of emissions. J. Geophys. Res.: Oceans **104**: 20703–20711. doi:10.1029/1999JC900148

Jerrem, K., T. C. Weber, and J. Beaudion. 2015. Split-beam echosounder observations of natural methane seep variability in the northern Gulf of Mexico. Geochem. Geophys. Geosyst. doi:10.1002/2014GC005429

Judd, A., G. Davies, J. Wilson, R. Holmes, G. Baron, and I. Bryden. 1997. Contributions to atmospheric methane by natural seepages on the UK continental shelf. Mar. Geol. **137**: 165–189. doi:10.1016/S0025-3227(96)00087-4

Judd, A. G., and M. Hovland. 2007. Seabed Fluid Flow. Cambridge Univ. Press, 360 p.

Knies, J., E. Damm, J. Gutt, U. Mann, and L. Ointurier. 2004. Near-surface hydrocarbon anomalies in shelf sediments off Spitsbergen: Evidences for past seepages. Geochem. Geophys. Geosyst. **5**: Q06003. doi:10.1029/2003GC000687

Kossel, E., N. Bigalke, E. Piñero, and M. Haeckel. 2013. The SUGAR Toolbox—a library of numerical algorithms and data for modelling of gas hydrate systems and marine environments, Bremenhaven, PANGEA. GEOMAR Report (N. Ser.), 8, 160 p. doi:10.3289/GEOMAR_REP_NS_8_2013.PANGAEA

Leblond, I., C. Scalabrin, and L. Berger. 2014. Acoustic monitoring of gas emissions from the seafloor. Part I: Quantifying the volumetric flow of bubbles. Mar. Geophys. Res. **35**: 191–210. doi:10.1007/s11001-014-9223-y

Lefeuvre, P. 2002. Fish species identification using image analysis of echo-sounder images. MSc. thesis. Univ. of Newfoundland.

Leifer, I., and D. Culling. 2010. Formation of seep bubble plumes in the Coal Oil Point seep field. Geo-Mar. Lett. **30**: 339–353. doi:10.1007/s00367-010-0187-x

Leifer, I., and R. K. Patro. 2002. The bubble mechanism for methane transport from the shallow sea bed to the surface: A review and sensitivity study. Cont. Shelf. Res. **22**: 2409–2428. doi:10.1016/S0278-4343(02)00065-1

Leifer, I., R. K. Patro, and P. Bowyer. 2000. A study on the temperature variation of rise velocity for large clean bubbles. J. Atmos. Ocean. Technol. **17**: 1392–1402. doi:10.1175/1520-0426(2000)0172.0.CO;2

Lewis, K. B., and B. A. Marshall. 1996. Seep faunas and other indicators of methane-rich dewatering on New Zealand convergent margins. N. Z. J. Geol. Geol. Geophys. **39**: 181–200. doi:10.1080/00288306.1996.9514704

Lorenson, T. D., I. Leifer, F. L. Wong, R. J. Rosenbauer, P. L. Campbell, A. Lam, F. D. Hostettler, J. Greinert, D. P. Finlayson, E. S. Bradley, and B. P. Luyendyk. 2011. Biomarker chemistry and flux quantification methods for

natural petroleum seeps and produced oils, offshore southern California: U.S. Geological Survey Scientific Investigations Report 2011-5210, 45 p. and OCS Study BOEM 2011016.

Lurton, X. 2002. An introduction to underwater acoustics: Principles and applications. Springer.

McGinnis, D. F., J. Greinert, Y. Artemov, S. E. Beaubien, and A. Wüest. 2006. Fate of rising methane bubbles in stratified waters: How much methane reaches the atmosphere? J. Geophys. Res.: Oceans **111**: C09007. doi:10.1029/2005JC003183

McGovern, C. 2012. Video-based quantification of gas bubble fluxes from the seafloor offshore western Svalbard. Msc. thesis, Univ. of Bremen.

Medwin, H. 1977. Counting bubbles acoustically. A review. Ultrasonics **7**: 13. doi:10.1016/0041-624X(77)90005-1

Medwin, H., and C. S. Clay. 1998. Bubbles, Chapter 8, p. 287–347. Fundamentals of Acoustical Oceanography. Academic Press.

Mendelson, H. D. 1967. The prediction of bubble terminal velocities from wave theory. AIChE J. **13**: 250–253. doi:10.1002/aic.690130213

Merewether, R., M. S. Olsson, and P. Lonsdale. 1985. Acoustically detected hydrocarbon plumes rising from 2-km depths in Guaymas Basin, Gulf of California. J. Geophys. Res.: Solid Earth **90**: 3075–3085. doi:10.1029/JB090iB04p03075

Minnaert, M. 1933. XVI. On musical air-bubbles and the sounds of running water. Philos. Mag. **16**: 235–248. doi:10.1080/14786443309462277

Muyakshin, S., and E. Sauter. 2010. The hydroacoustic method for the quantification of the gas flux from a submersed bubble plume. Oceanology **50**: 995–1001. doi:10.1134/S0001437010060202

Naudts, L., J. Greinert, Y. Artemov, P. Staelens, J. Poort, P. Van Rensbergen, and Marc De Batist. 2006. Geological and morphological setting of 2778 methane seeps in the Dnepr paleo-delta, northwestern Black Sea. Mar. Geol. **227**: 177–199. doi:10.1016/j.margeo.2005.10.005

Nikolovska, A., H. Sahling, and G. Bohrmann. 2008. Hydroacoustic methodology for detection, localization, and quantification of gas bubbles rising from the seafloor at gas seeps from the eastern Black Sea. Geochem. Geophy. Geosy. **9**: Q10010. doi:10.1029/2008GC002118

Obzhirov, A., R. Shakirov, A. Salyuk, E. Suess, N. Biebow, and A. Salomatin. 2004. Relations between methane venting, geological structure and seismo-tectonics in the Okhotsk Sea. Geo-Mar. Lett. **24**: 135–139. doi:10.1007/s00367-004-0175-0

Ostrovsky, I. 2003. Methane bubbles in Lake Kinneret: Quantification and temporal and spatial heterogeneity. Limnol. Oceanogr. **48**: 1030–1036. doi:10.4319/lo.2003.48.3.1030

Ostrovsky, I. 2009. Hydroacoustic assessment of fish abundance in the presence of gas bubbles. Limnol. Oceanogr.: Methods **7**: 309–318. doi:10.4319/lom.2009.7.309

Ostrovsky, I., D. Mcginnis, L. Lapidus, and W. Eckert. 2008. Quantifying gas ebullition with echosounder: The role of methane transport by bubbles in a medium-sized lake. Limnol. Oceanogr.: Methods **6**: 18. doi:10.4319/lom.2008.6.105

Paull, C. K., W. Ussler, W. S. Borowski, and F. N. Spiess. 1995. Methane-rich plumes on the Carolina continental rise: Associations with gas hydrates. Geology **23**: 89–92. doi:10.1130/0091-7613(1995)023<0089:MRPOTC>2.3.CO;2

Polikarpov, G. G., and V. N. Egorov. 1989. Evidence of the gas bubble streams from the Black Sea bottom, Visnik AN. UkrSSR **10**: 108.

Prosperetti, A., N. Q. Lu, and H. S. Kim. 1993. Active and passive acoustic behavior of bubble clouds at the ocean's surface. J. Acoust. Soc. Am. **93**: 3117–3127. doi:10.1121/1.405696

Quigley, D. C., J. Scott Hornafius, B. P. Luyendyk, R. D. Francis, J. Clark, and L. Washburn. 1999. Decrease in natural marine hydrocarbon seepage near Coal Oil Point, California, associated with offshore oil production. Geology **27**: 1047–1050. doi:10.1130/0091-7613(1999)027<1047:DINMHS>2.3.CO;2

Rajan, A., J. Mienert, and S. Bünz. 2012. Acoustic evidence for a gas migration and release system in Arctic glaciated continental margins offshore NW-Svalbard. Mar. Petrol. Geol. **32**: 36–49. doi:10,1016/j.marpetgeo.2011.12.008

Rehder, G., I. Leifer, P. G. Brewer, G. Friederich, and E. T. Peltzer. 2009. Controls on methane bubble dissolution inside and outside the hydrate stability field from open ocean field experiments and numerical modeling. Mar. Chem. **114**: 19–30. doi:10.1016/j.marchem.2009.03.004

Römer, M., H. Sahling, V. Spieß, and G. Bohrmann. 2011. The role of gas bubble emissions at deep-water cold seep systems: An example from the Makran continental margin, offshore Pakistan. Proceedings of the 7th International Conference on Gas Hydrates (ICGH 2011), Edinburgh, Scotland, United Kingdom, July 17–21, 2011, 8 pp.

Römer, M., H. Sahling, T. Pape, A. Bahr, T. Feseker, P. Wintersteller, and G. Bohrmann. 2012a. Geological control and magnitude of methane ebullition from a high-flux seep area in the Black Sea—the Kerch seep area. Mar. Geol. **319–322**: 57–74. doi:10.1016/j.margeo.2012.07.005

Römer, M., H. Sahling, T. Pape, G. Bohrmann, and V. Spieß. 2012b. Quantification of gas bubble emissions from submarine hydrocarbon seeps at the Makran continental margin (offshore Pakistan). J. Geophys. Res.: Oceans **117**: C10015. doi:10.1029/2011JC007424

Sahling, H., and others. 2009. Vodyanitskii mud volcano, Sorokin trough, Black Sea: Geological characterization and quantification of gas bubble streams. Mar. Petrol. Geol. **26**: 1799–1811. doi:10.1016/j.marpetgeo.2009.01.010

Sahling, H., and others. 2014. Gas emissions at the continental margin west off Svalbard: Mapping, sampling, and quantification. Biogeosciences **11**, 7189–7234.

Salmi, M. S., H. P. Johnson, I. Leifer, and J. E. Keister. 2011. Behavior of methane seep bubbles over a pockmark on the Cascadia continental margin. Geosphere **7**: 1273–1283. doi: 10.1130/GES00648.1

Sauter, E. J., and others. 2006. Methane discharge from a deep-sea submarine mud volcano into the upper water column by gas hydrate-coated methane bubbles. Earth Planet. Sci. Lett. **243**: 354–365. doi:10.1016/j.epsl.2006.01.041

Schneider Von Deimling, J., G. Rehder, J. Greinert, D. F. Mcginnnis, A. Boetius, and P. Linke. 2011. Quantification of seep-related methane gas emissions at Tommeliten, North Sea. Cont. Shelf Res. **31**: 867–878. doi:10.1016/j.csr.2011.02.012

Shakhova, N., and I. Semiletov. 2007. Methane release and coastal environment in the East Siberian Arctic shelf. J. Marine. Syst. **66**: 227–243. doi:10.1016/j.marsys.2006.06.006

Shakhova, N., and others. 2014. Ebullition and storm-induced methane release from the East Siberian Arctic Shelf. Nat. Geosci. **7**: 64–70. doi:10.1038/ngeo2007

Simmonds, J., and D. N. MacLennan. 2005. Fisheries Acoustics: Theory and Practice. Wiley.

Smith, A. J.; Mienert, J., Bünz, S., and Greinert, J. 2014. Thermogenic methane injection via bubble transport into the upper Arctic Ocean from the hydrate-charged Vestnesa Ridge, Svalbard. Geochem. Geophys. Geosyst. **15**: 1945–1959. doi.org/10.1002/2013GC005179

Solomon, E. A., M. Kastner, H. Jannasch, G. Robertson, and Y. Weinstein. 2008. Dynamic fluid flow and chemical fluxes associated with a seafloor gas hydrate deposit on the northern Gulf of Mexico slope. Earth Planet. Sci. Lett. **270**: 95–105. doi:10.1016/j.epsl.2008.03.024

Solomon, E. A., M. Kastner, I. R. MacDonald, and I. Leifer. 2009. Considerable methane fluxes to the atmosphere from hydrocarbon seeps in the Gulf of Mexico. Nat. Geosci. **2**: 561–565. doi:10.1038/ngeo574

Stanton, T. K. 1989. Simple approximate formulas for backscattering of soundby spherical and elongated objects. J. Acoust. Soc. Am. **86**: 1499–15l0. doi:10.1121/1.398711

Strasberg, M. 1953. The pulsation frequency of non-spherical gas bubbles in liquids. J. Acoust. Soc. Am. **25**: 536–537. doi:10.1121/1.1907076

Talukder, R. A., and others. 2013. Natural hydrocarbon seepage on the continental slope to the east of Mississippi Canyon in the northern Gulf of Mexico. Geochem. Geophy. Geosyst. **14**: 1940–1956. doi:10.1002/ggge.20130

Thuraisingham, R. A. 1997. New expressions of acoustic cross-sections of a single bubble in the monopole bubble theory. Ultrasonics **35**: 407–409. doi:10.1016/S0041-624X(97)00021-8

Weber, T. C., K. Jerram, Y. Rzhanov, L. Mayer, and D. Lovalvo. 2013. Acoustic and optical observations of methane gas seeps in the Gulf of Mexico. In Proceedings of Meetings on Acoustics, Acoustical Society of America **19**: p075046.

Weber, T. C., L. Mayer, K. Jerram, J. Beaudoin, and Y. Rzhanov. 2014. Acoustic estimates of methane gas flux from the seabed in a 6000 km^2 region in the Northern Gulf of Mexico. Geochem. Geophy. Geosyst. **15**: 1911–1925. doi:10.1002/2014GC005271

Wessel, P., W. H. F. Smith, R. Scharroo, J. Luis, and F. Wobbe. 2013. Generic MappingTools: Improved Version Released. Eos, Trans. Am. Geophys. Union **94**: 409–410. doi:10.1002/2013EO450001

Westbrook, G. K., and others. 2009. Escape of methane gas from the seabed along the West Spitsbergen continental margin. Geophys. Res. Lett. **36**: L15608. doi:10.1029/2009GL039191

Wildt, R. 1946. Acoustic theory of bubbles, Chapter 28, p. 460–477. Physics of Sound in the Sea, NDRC Summary Technical Report Div. 6, Volume 8.

Woolf, D. K. 1993. Bubbles and the air-sea transfer velocity of gases. Atmos. Ocean **31**: 517–540. doi:10.1080/07055900.1993.9649484

Woolf, D. K., and S. Thorpe. 1991. Bubbles and the air-sea exchange of gases in near-saturation conditions. J. Mar. Res. **49**: 435–466. doi:10.1357/002224091784995765

Acknowledgments

We are thankful for the support received during several surveys by the master and his crew of RV Helmer Hanssen from UiT the Arctic University of Norway, N-9037 Tromsø. M. Veloso and J. Greinert both received support via COST Action ES0902 (PERGAMON) to join research cruises to acquire data. M. Veloso thanks the ERASMUS Mundus program of the EU (grant VECCEU) and the "Becas de doctorado en el extranjero, BECAS CHILE: CONICYT PAI/INDUSTRIA 79090016" program of the Chilean government. Edna Hütten is thanked for proof-reading the manuscript and Ira Leifer for giving access to his MATLAB script for calculating bubble rising speeds. The research is also part of the Centre of Excellence: Arctic Gas Hydrate, Environment and Climate (CAGE) funded by the Norwegian Research Council (grant No. 223259).Our warmest thanks go to Sergei Muyakshin who kindly discussed his methodology with us during a visit at GEOMAR.

Submitted 22 May 2014
Revised 22 February 2015
Accepted 1 March 2015

Associate editor: Paul Kemp